A Foundational Generative Model for Cross-platform Unified Enhancement of Spatial Transcriptomics

Xiaofei Wang[1*]; Hanyu Liu[2*]; Ningfeng Que[3*]; Chenyang Tao[1]; Yu Jiang[4]; Yixuan Jiang[5]; Pinan Zhu[5]; Junze Zhu[6]; Xiaoyang Li[5]; Jianguo Xu[4]; Stephen Price[1]; Jianzhong Xi[3†]; Xinjie Wang[7†]; Chao Li[1,2,8,9†]

1. Department of Clinical Neurosciences, University of Cambridge, UK

2. School of Science and Engineering, University of Dundee, UK

3. State Key Laboratory of Natural and Biomimetic Drugs, Department of Biomedical Engineering, College of Future Technology, Peking University, Beijing, China

4. Department of Neurosurgery, West China Hospital, Sichuan University, Chengdu, China

5. College of Medicine and Biological Information Engineering, Northeastern University, Shenyang, China

6. School of Computer Science and Technology, Tongji University, Shanghai, China

7. State Key Laboratory of Genome and Multi-omics Technologies, Genome Analysis Laboratory of the Ministry of Agriculture and Rural Affairs, Agricultural Genomics Institute at Shenzhen, Chinese Academy of Agricultural Sciences, Shenzhen, China

8. Department of Applied Mathematics and Theoretical Physics, University of Cambridge, UK

9. School of Medicine, University of Dundee, UK

*Equal contributions

†Correspondence: Chao Li (cl647@cam.ac.uk); Xinjie Wang (wangxinjie@caas.cn); Jianzhong Xi (jzxi@pku.edu.cn)

Abstract

Spatial transcriptomics (ST) platforms are limited by spatial resolution, sensitivity to low expression levels, alignment with tissue structures, and the balance across tissue complexity. Computational enhancement typically targets a single challenge, e.g., super-resolution using hematoxylin and eosin (H&E) images or sensitivity enhancement with single-cell RNA sequencing (scRNA-seq). However, most ignore the interdependence across challenges, yielding biologically inconsistent enhancement. Here we introduce FOCUS, a foundational generative model for unified ST enhancement, conditioned on H&E images, scRNA-seq references, and spatial co-expression priors. With large-scale pretrained encoders, FOCUS uses a modular design for *multimodal* integration and a cross-challenge coordination strategy to target co-occurring challenges, enabling joint optimization. FOCUS was trained and comprehensively benchmarked on >1.7 million H&E-ST pairs and >5.8 million single-cell profiles, demonstrating state-of-the-art performance across ten ST platforms, on both individual and coupled challenges. The real-world utility and generalizability were validated on a rare suprasellar tumor, papillary craniopharyngioma, and an unseen ST platform (Open-ST) for primary and metastatic head and neck squamous cell carcinoma.

Introduction

Spatial transcriptomics (ST) enables *in situ* profiling across tissues; however, recent benchmarks[1–3] reveal persistent co-occurring limitations across platforms, including spatial resolution, sensitivity to low expression, alignment with tissue structures, and profiling balance across tissue complexity, hindering its biological utility and interpretability.

First, there is an inherent trade-off between spatial resolution and sequencing depth. Recent platforms, e.g., VisiumHD, offer subcellular resolution but at the expense of per-spot transcript counts, limiting profiling accuracy. **Second**, due to limited tissue RNA, inefficient capture, and throughput bottleneck[3,4], existing platforms remain low in sensitivity, especially for lowly expressed genes. Profiling bias persists despite experimental strategies such as increasing barcoding density[5]. **Third**, spatial fidelity is often compromised by artifacts arising from lateral mRNA diffusion during tissue permeabilization in sequencing-based ST and from repeated rounds of hybridization in imaging-based ST[2,3,6,7]. The resulting spatial distortions complicate morphology-guided tasks. **Finally**, in complex tissues such as cancer, cellular packing leads to the blending of transcripts from neighboring cells, even when there is perfect alignment with tissue structures[8–10]. This signal mixing reduces profiling precision for rare cells or subtle niches.

Emerging studies have sought to address these challenges by including additional modalities to enhance ST. One strategy leverages paired hematoxylin and eosin (H&E)-stained images to enhance spatial resolution[11–13] or spatially align molecular signals with tissue structure[14–16]. Other strategies involve single-cell RNA sequencing (scRNA-seq) to enhance profiling sensitivity to low expression[4,17,18]. However, each modality carries intrinsic limitations: scRNA-seq is often profiled on different samples from ST and may not reflect the cell composition or tissue architecture of ST, whereas H&E images, though structurally detailed, lack the molecular resolution to distinguish morphologically similar but transcriptionally distinct cells. Integrating complementary modalities, therefore, represents a promising yet under-explored opportunity to enhance ST. This integration is particularly important since major ST challenges are often **coupled**. For example, low spatial resolution blurs tissue boundaries, leading to poor alignment with tissue structures,

while high tissue complexity, e.g., high cell density, can restrict the capture of per-cell molecules, limiting sensitivity to low expression levels. Without unified optimization across challenges, existing methods risk yielding biologically inconsistent reconstructions.

Generative models, particularly diffusion models[19–22], promise to tackle multiple ST challenges by conditioning on complementary modalities. In parallel, recent advances in foundational models[23], enabled by large-scale pretraining and modular architectures, can generalize across domains and tasks with lightweight fine-tuning, supporting cross-platform ST enhancement. Together, these advances motivate a foundational generative strategy for joint, cross-challenge ST reconstruction. Here, we propose FOCUS (FOundational generative model for Cross-platform Unified enhancement of Spatial transcriptomics), a diffusion-based framework that reconstructs high-quality ST by jointly optimizing multiple objectives. Built on foundational pre-trained encoders[23,24], FOCUS integrates paired H&E images, cell masks, scRNA-seq references, and spatial co-expression priors to address multiple ST challenges within a single model. Through challenge-tailored modules and explicit cross-challenge coordination, FOCUS transforms fragmented, challenge-specific enhancements into unified ST reconstruction.

FOCUS is comprehensively benchmarked on ten ST platforms (including sequencing- and imaging-based technologies), with over 1.7 million paired H&E-ST patches and 5.8 million scRNA-seq cell profiles. It outperforms both native platforms and state-of-the-art methods, consistently demonstrating improvements across individual and coupled challenges across scales (global, regional, and cellular), as well as on downstream tasks such as spatial domain characterization and cell-cell co-localization. Finally, we utilized FOCUS on two real-world scenarios, thereby validating its strong generalization. FOCUS is open source and publicly available at https://github.com/LHY1007/FOCUS/.

Results

2.1 Study overview

In this study, we proposed a foundational generative model, FOCUS, to jointly enhance ST spatial resolution, sensitivity to low expression, alignment with tissue structures, and profiling balance across tissue complexity in a single, unified framework (Fig. 1a, Extended Figs. 1-2). Built on a diffusion-based backbone, FOCUS adopts a foundational model design, including large-scale pretraining and challenge-tailored modules, as well as coordinated cross-challenge interactions to achieve unified optimization across all challenges.

FOCUS was trained and benchmarked across eight sequencing-based and two imaging-based platforms, on both human (*Homo sapiens*) and mouse (*Mus musculus*) specimens (Fig. 1b). Comprehensive validation was performed across individual and coupled challenges (Fig. 1c). Furthermore, we fine-tuned FOCUS on datasets from unseen platform or tissue context: **(i)** primary and metastatic human head and neck squamous cell carcinoma (HNSCC), profiled from a novel ST platform (Open-ST)[25] with consecutive tissue sections to evaluate cross-platform generalization, and **(ii)** papillary craniopharyngioma (PCP), a rare heterogeneous suprasellar tumor, testing model's ability to localize disease-relevant transcriptional patterns for real-world utility.

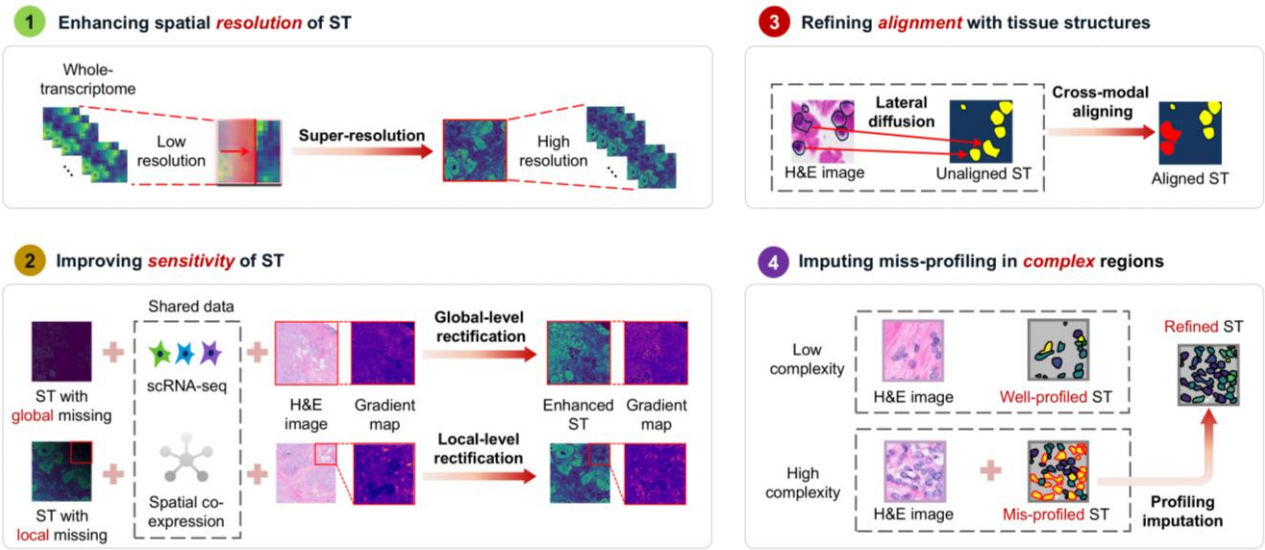

Extended Fig. 1 | Schematic illustration of major challenges in current ST platforms targeted by computational methods: (1) coarse spatial resolution, (2) limited sensitivity to low expression, (3) misalignment with tissue structures, and (4) miss-profiling in complex tissues.

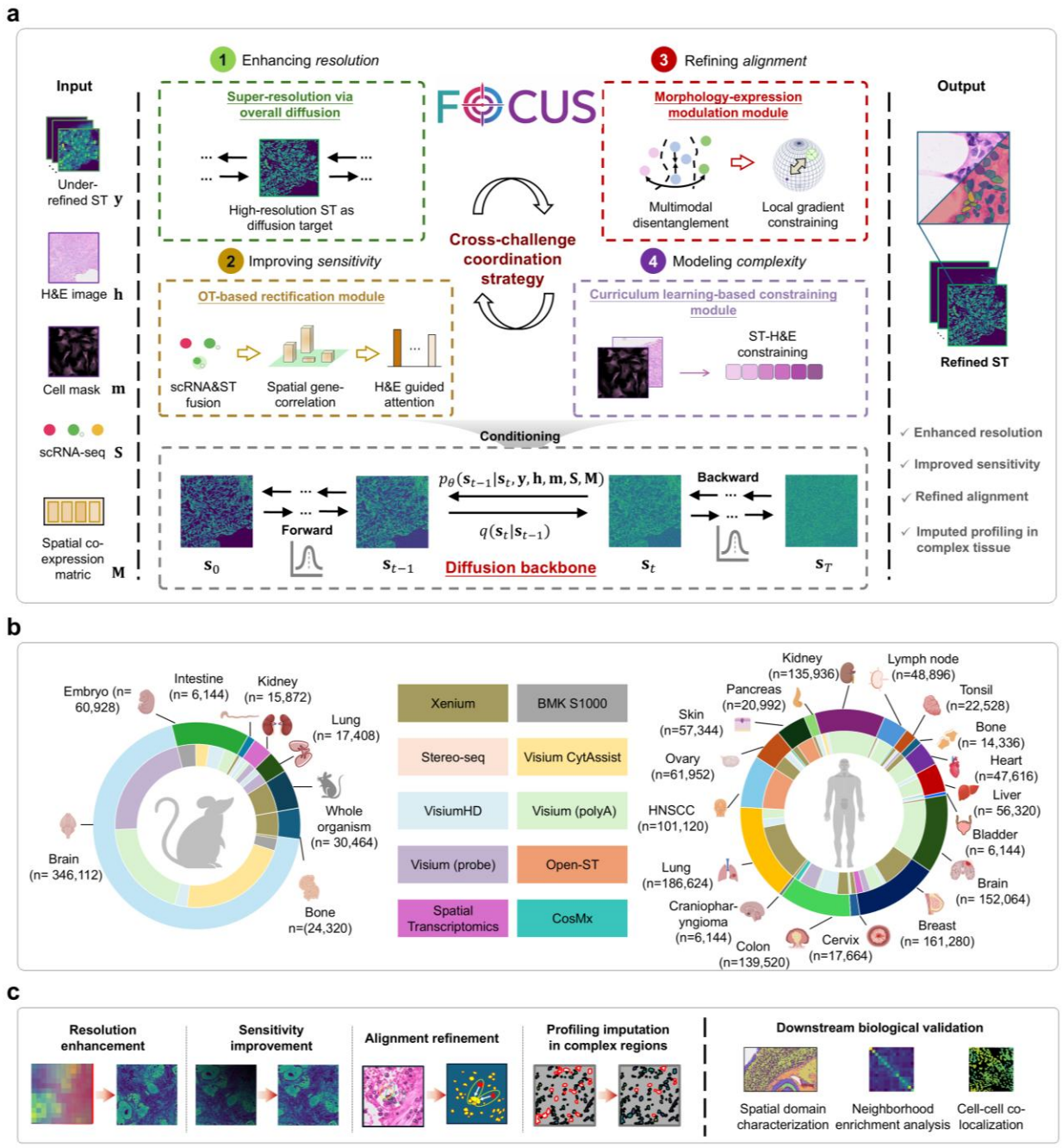

Fig. 1 | Model design and validation for ST enhancement. a, Model overview. FOCUS is a foundational generative model that leverages the modular architecture and multimodal encoders[23,24] pretrained on large-scale, cross-tissue ST and H&E data. Built on the diffusion model, it integrates multimodal conditions as inputs, including raw ST maps, paired H&E images with cell segmentation masks, scRNA-seq references, and spatial gene co-expression matrices. Each challenge is addressed through tailored modules, with a cross-challenge coordination strategy enabling module

interaction for coherent improvement across challenges. **b**, Large-scale, cross-platform multimodal dataset. In total, we assemble 6,788 paired ST-H&E images (corresponding to over 1.7 million patches) with matched cell segmentation masks, referenced scRNA-seq from public sources (over 5.8 million scRNA-seq cell profiles; Table S1), and pre-computed spatial gene co-expression matrices. The data collection spans ten ST platforms, including eight sequencing-based (Visium [probe-based and polyA-based], Visium Cytassist, VisiumHD, Spatial Transcriptomics, Stereo-seq, BMK S1000, and Open-ST) and two imaging-based (Xenium and CosMx) platforms, and two species (human and mouse), comprising 17 normal and 17 cancer tissues, with whole-transcriptome profiles available for both species. **c,** Benchmarking and validation across challenges and downstream tasks, including spatial domain characterization, neighborhood enrichment analysis, and cell-cell co-localization.

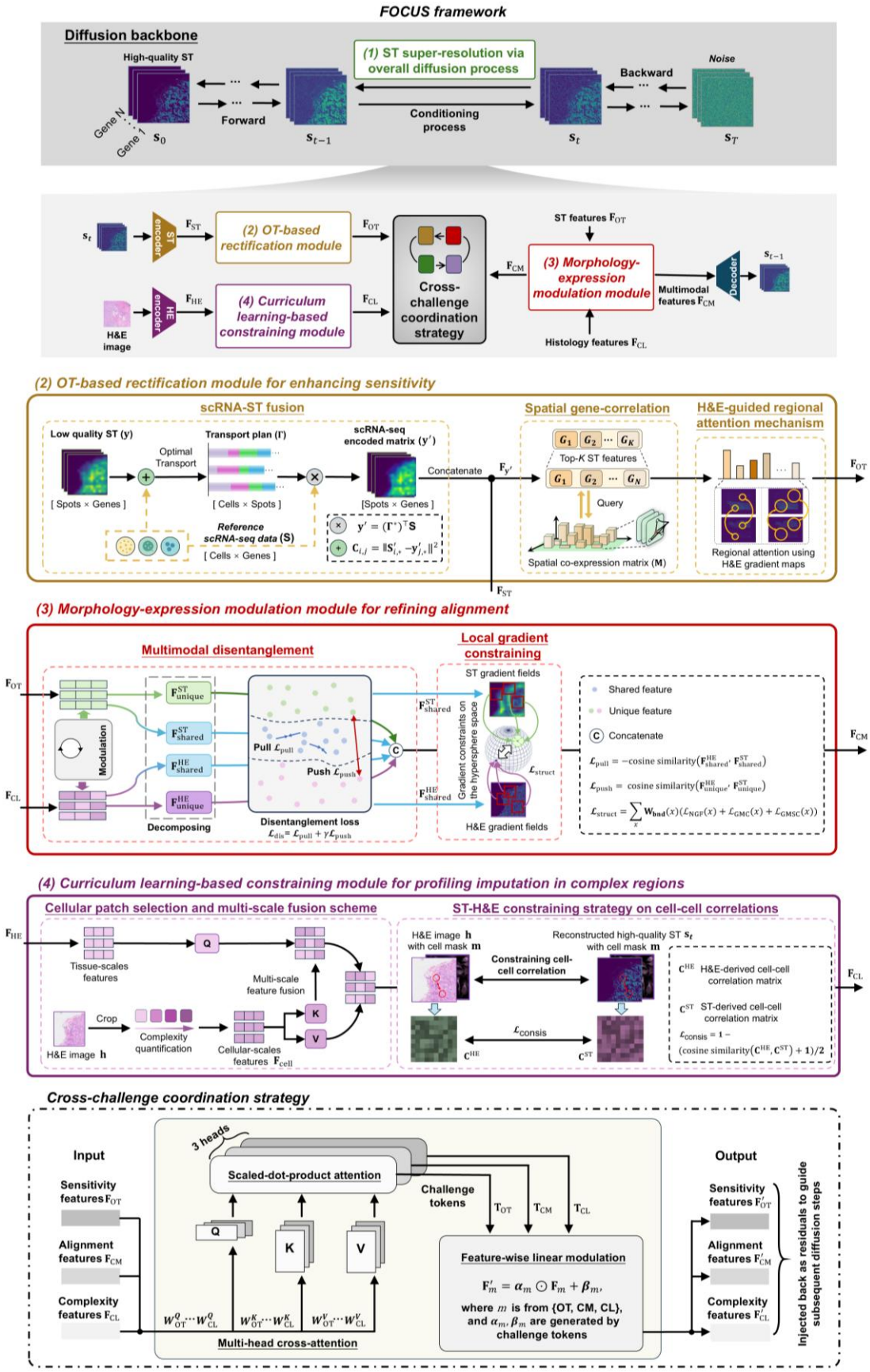
FOCUS framework
Diffusion backbone
High-quality ST
Gene N
Gene 1
Forward
(1) ST super-resolution via overall diffusion process
Conditioning process
Backward
Noise
(2) OT-based rectification module
(3) Morphology-expression modulation module
(4) Curriculum learning-based constraining module
Cross-challenge coordination strategy
ST encoder
HE encoder
H&E image
ST features
Histology features
Multimodal features
Decoder
(2) OT-based rectification module for enhancing sensitivity
scRNA-ST fusion
Low quality ST (y)
Optimal Transport
Transport plan (Γ)
scRNA-seq encoded matrix (y′)
Concatenate
Reference scRNA-seq data (S)
Spatial gene-correlation
Top-K ST features
Query
Spatial co-expression matrix (M)
H&E-guided regional attention mechanism
Regional attention using H&E gradient maps
(3) Morphology-expression modulation module for refining alignment
Multimodal disentanglement
Modulation
Decomposing
Pull
Push
Disentanglement loss
Local gradient constraining
ST gradient fields
H&E gradient fields
Gradient constraints on the hypersphere space
Shared feature
Unique feature
Concatenate
(4) Curriculum learning-based constraining module for profiling imputation in complex regions
Cellular patch selection and multi-scale fusion scheme
Tissue-scales features
Multi-scale feature fusion
Crop
Complexity quantification
Cellular-scales features
ST-H&E constraining strategy on cell-cell correlations
H&E image with cell mask
Reconstructed high-quality ST with cell mask
Constraining cell-cell correlation
H&E-derived cell-cell correlation matrix
ST-derived cell-cell correlation matrix
Cross-challenge coordination strategy
Input
Sensitivity features
Alignment features
Complexity features
3 heads
Scaled-dot-product attention
Challenge tokens
Feature-wise linear modulation
where m is from {OT, CM, CL}, and α_m, β_m are generated by challenge tokens
Multi-head cross-attention
Output
Injected back as residuals to guide subsequent diffusion steps

Extended Fig. 2 | Illustration of the FOCUS framework. FOCUS builds on a diffusion backbone. In the forward process, high-quality ST $\mathbf{s}_0$ is gradually added with noise to derive $\mathbf{s}_T$ in T steps, and the reverse process learns to denoise. At each reverse step t, FOCUS learns to predict $\mathbf{s}_{t-1}$ from $\mathbf{s}_t$ within a conditioning process. This process uses multimodal pretrained encoders[23,24] (encoding ST features $\mathbf{s}_t$ and H&E image $\mathbf{h}$ to $\mathbf{F}_{\mathrm{ST}}$ and $\mathbf{F}_{\mathrm{HE}}$, respectively), and comprises both a challenge-tailored design and a cross-challenge coordination strategy: **(1)** By taking high-resolution ST maps as the diffusion generation target, FOCUS is able to achieve ST spatial resolution enhancement. **(2)** The optimal transport (OT)-based rectification module enhances sensitivity to low expression, with output features of $\mathbf{F}_{\mathrm{OT}}$. First, the raw ST $\mathbf{y}$ is mapped with the scRNA-seq reference $\mathbf{S}$ by using an OT-based cell-spot mapping approach. Afterwards, the resulting transport plan $\mathbf{\Gamma}$ maps high-sensitivity single-cell expression onto the ST spots, producing the scRNA-informed ST feature $\mathbf{F}_{\mathbf{y}'}$. We then refine $\mathbf{F}_{\mathbf{y}'}$ using pre-computed spatial co-expression matrices $\mathbf{M}$ to reflect gene-gene spatial relationships. Finally, to improve sensitivity in morphologically distinct regions, we introduce an H&E-guided regional attention mechanism that upweights areas with strong H&E gradients, indicative of distinct tissue structures. **(3)** Morphology-expression modulation module refines alignment with tissue structures, with output features of $\mathbf{F}_{\mathrm{CM}}$. First, a multimodal disentanglement strategy decomposes the ST and H&E features ($\mathbf{F}_{\mathrm{OT}}$ and $\mathbf{F}_{\mathrm{CL}}$) into shared and modality-specific components. This decomposition is achieved through a disentanglement loss $\mathcal{L}_{\mathrm{dis}}$, which separates modality-shared structural features from modality-specific patterns between H&E images and ST maps. Based on the shared features, we further utilize the local gradient constraining (via the structural loss $\mathcal{L}_{\mathrm{struct}}$) to refine the misalignment with tissue structures. **(4)** Curriculum learning-based constraining module balances profiling across tissue complexity, with output features of $\mathbf{F}_{\mathrm{CL}}$. We first quantify complexity using H&E images, which are then used to gradually select complex areas during curriculum learning. Within the selected areas, we further introduce an ST-H&E constraining strategy to improve expression precision, where the ST-derived cell-cell correlations are constrained to match H&E-derived correlations via a consistency loss $\mathcal{L}_{\mathrm{consis}}$. **Cross-challenge coordination strategy**: To enable interaction and joint enhancement across challenges, features from each module ($\mathbf{F}_{\mathrm{OT}}, \mathbf{F}_{\mathrm{CL}}, \mathbf{F}_{\mathrm{CM}}$) are converted into compact tokens, interacting via multi-head cross-attention. The resulting tokens produce feature-wise scaling and shifting coefficients that recalibrate features across modules. The final coordinated features ($\mathbf{F}'_{\mathrm{OT}}, \mathbf{F}'_{\mathrm{CL}}, \mathbf{F}'_{\mathrm{CM}}$) are reintroduced into the conditioning process as residuals to guide subsequent diffusion steps.

2.2 Model, data, and benchmarking

2.2.1 Model design

Backbone and coordinated modular design

Generative models are designed to learn underlying distributions and can naturally incorporate multimodal conditions, enabling to tackle multiple ST challenges within a single framework. Compared to conventional models[26], diffusion models provide stable training on heterogeneous, multi-platform ST by gradually adding noise to the data and learning to reconstruct the original signals in a reverse process[27]. With high-resolution ST as the generation target, diffusion models naturally support resolution enhancement.

Built on the diffusion model, FOCUS further adopts a foundational model design, including the modular architecture and large-scale pretraining, enabling unified and flexible ST enhancement. Specifically, FOCUS introduces challenge-tailored modules to integrate complementary modalities, including paired H&E images, cell segmentation masks, scRNA-seq references, and spatial gene co-expression priors (Extended Fig. 2). To ensure comprehensive representation across modalities, FOCUS is built on two large-scale pretrained encoders to capture morphological and transcriptional patterns: **1)** an H&E encoder[23] pretrained on 1.3 billion patches covering 31 tissues, and **2)** an ST encoder[24] pretrained on 30 million spatially profiled spots. A cross-challenge coordination strategy is embedded in the reverse diffusion process, enabling selective module combination and providing flexibility.

Optimal transport (OT)-based rectification module

To boost sensitivity to low-expression levels, we first designed an OT-based cell-spot mapping strategy that fuses ST with scRNA-seq references, thereby transferring high-sensitivity single-cell expression onto ST spots. Motivated by our observation that adding spatial context better represents gene correlations (Extended Fig. 3a-b; Supplementary section 1), we further devise a spatial gene-correlation strategy that leverages pre-computed spatial co-expression matrices to improve recovery of lowly captured genes. To further improve local sensitivity in morphologically distinct regions, we introduced an

H&E-guided regional attention mechanism that upweights areas with high H&E gradients indicative of distinct tissue structures during learning.

Morphology-expression modulation module

To improve misalignment with tissue structures, we devised a multimodal disentangling strategy, based on our finding that ST maps and H&E images exhibit high spatial consistency across cellular to tissue scales (Extended Fig. 3c). Based on this consistency, the disentanglement is designed to separate modality-shared structural features from modality-specific patterns between H&E images and ST maps, imposing local gradient constraints on the shared features to improve alignment with tissue structures.

Curriculum learning-based constraining module

To reduce transcript mixing in complex areas and improve profiling balance across tissue complexity, FOCUS first quantifies tissue complexity (considering both cell density and cell type diversity using H&E features; see Methods) and gradually focuses on more complex areas via curriculum learning. To further improve expression precision within complex regions, H&E-derived cell-cell correlations were used to refine ST-derived correlations, as H&E-based cellular morphology is relatively less affected by transcript mixing in complex tissue regions.

Cross-challenge coordination strategy

The cross-challenge coordination strategy further models co-occurring challenges (e.g., low spatial resolution with poor alignment with tissue structures shown in Fig. S1) inside the diffusion conditioning process (Extended Fig. 2). For each module, the generated features are compressed into module-specific tokens, with multi-head cross-attention applied over tokens, so that each module conditions its update on the others. The attended tokens are then converted to module-specific scaling and shifting coefficients that modulate the original feature maps, providing coordinated updates on modules. See Supplementary section 2 (Fig. S2) for an ablation analysis of the distinct modules and cross-challenge coordination strategy.

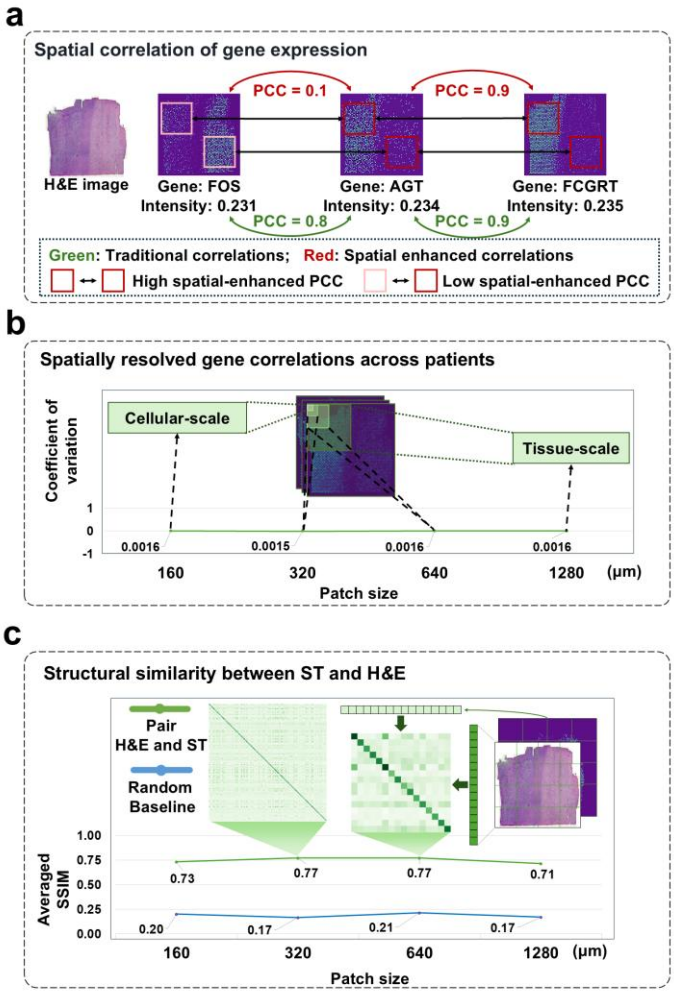

Extended Fig. 3 | Cross-gene and cross-modal correlation analysis supporting FOCUS modular designs. a, Spatial information refines traditional gene correlations. For example, in Xenium human breast cancer samples, the Pearson correlation coefficient (PCC) between *FOS* and *AGT* drops from 0.8 (global expression PCC) to 0.1 when spatial PCC is used, indicating that global expression correlations mask spatial patterns of gene co-expression. This implies that ST enhancement may benefit from considering spatial gene co-expression priors. **b,** The spatial gene co-expression patterns revealed in **a** are highly consistent across patients, as indicated by the low coefficient of variation (CV). This consistency suggests that shared spatial gene correlations can be leveraged across samples within the same tissue context. **c,** Average structure similarity index measure (SSIM) between paired H&E and ST patches (green) *versus* randomly matched patches (blue, baseline) across patch sizes. High SSIM values reflect strong structural consistency between ST and H&E images.

2.2.2 Datasets for training and validation

We assembled a large-scale, cross-modal dataset of 6,788 paired ST-H&E images (2,560 × 2,560 μm) and over 1.7 million patches (160 × 160 μm). Each tissue type is linked to corresponding scRNA-seq profiles (over 5.8 million reference cells) and our pre-

computed corresponding spatial gene co-expression matrices (Methods). Detailed dataset description is in Tables S1-3.

The dataset comprises 17 normal and 17 cancer tissues from human and mouse samples, profiled by sequencing-based: Visium (probe-based and polyA-based)[28], Visium CytAssist[29], and VisiumHD[30] (all Visium platforms are products of 10X Genomics), Spatial Transcriptomics[31] (Spatial Transcriptomics AB), Stereo-seq[32] (BGI), BMK S1000[33] (BMKGENE), and Open-ST[25], and image-based platforms: Xenium[34] (10X Genomics) and CosMx[35] (Nanostring). Detailed dataset and training/validation split are in Methods.

2.2.3 Benchmarking settings

We benchmarked FOCUS on four challenges, comparing both native platforms and challenge-specific baselines[1] (Sections 2.3-2.6). Detailed results across all platforms are presented in Tables S4-7. Further, we compared FOCUS with state-of-the-art foundational generative models adapted for ST, demonstrating the value of ST-specific design (Fig. S3; Supplementary sections 4).

[1] Definition of metrics used for evaluation for each challenge is in Supplementary section 3.

Resolution enhancement benchmarking

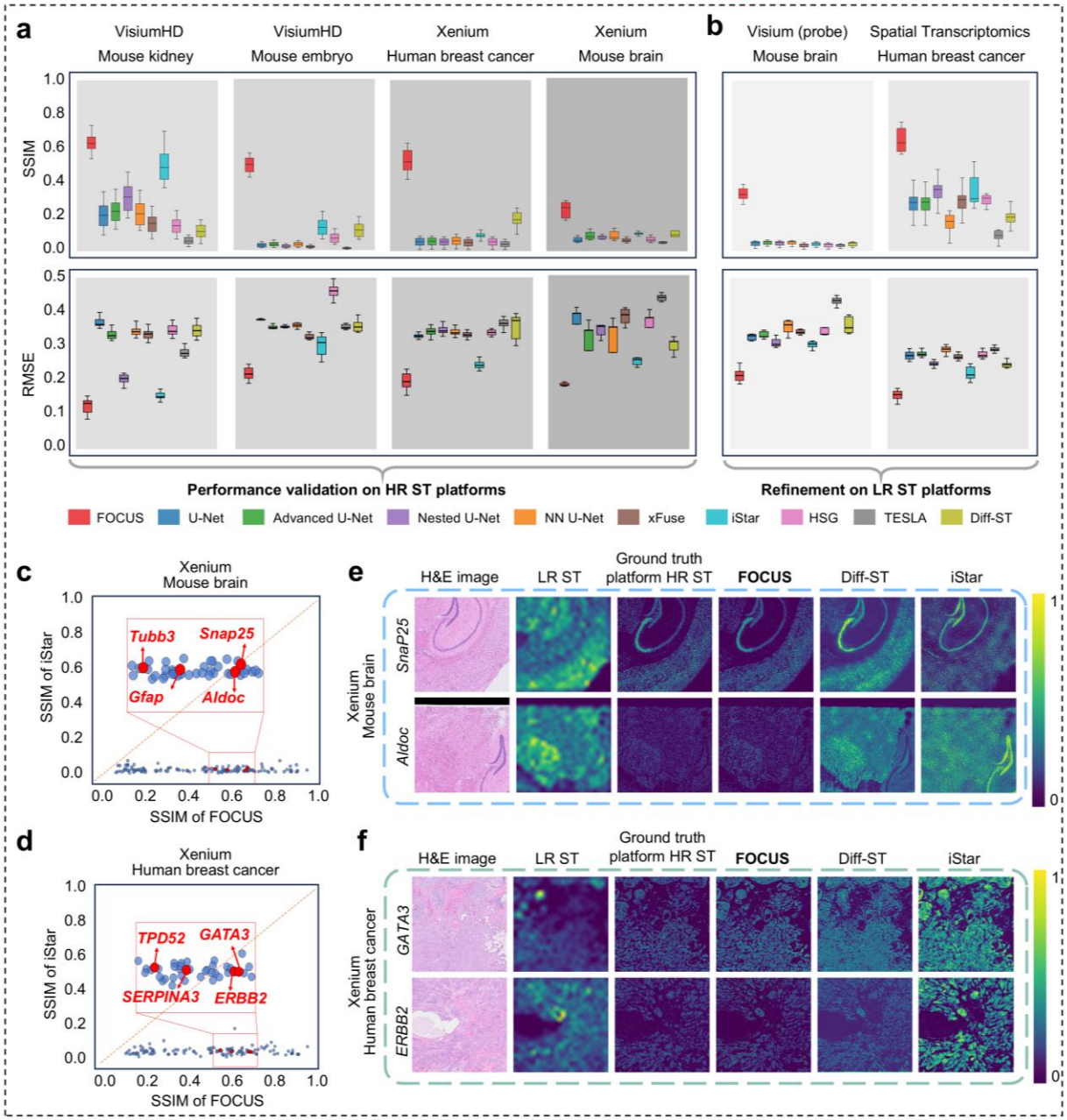

Improved spatial domain characterization with enhanced resolution

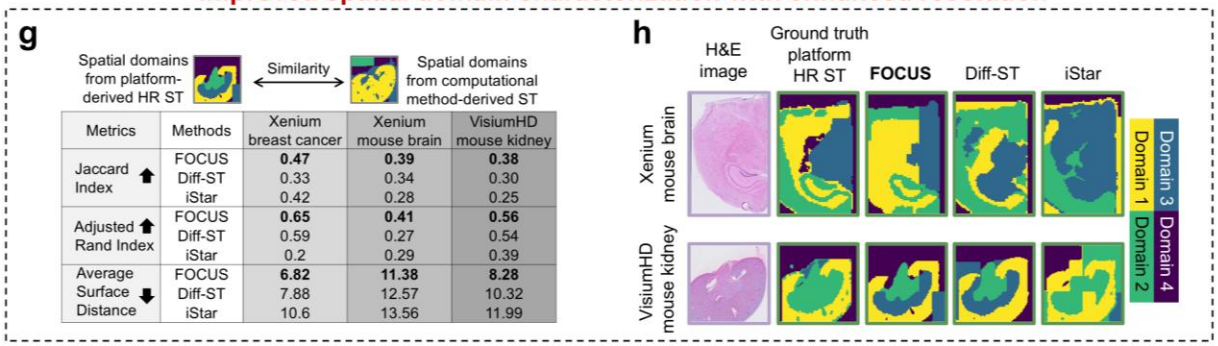

Metrics	Methods	Xenium breast cancer	Xenium mouse brain	VisiumHD mouse kidney
Jaccard Index ↑	FOCUS	**0.47**	**0.39**	**0.38**
	Diff-ST	0.33	0.34	0.30
	iStar	0.42	0.28	0.25
Adjusted Rand Index ↑	FOCUS	**0.65**	**0.41**	**0.56**
	Diff-ST	0.59	0.27	0.54
	iStar	0.2	0.29	0.39
Average Surface Distance ↓	FOCUS	**6.82**	**11.38**	**8.28**
	Diff-ST	7.88	12.57	10.32
	iStar	10.6	13.56	11.99

Fig. 2 | Evaluation of FOCUS in resolution enhancement. (**a-f**)**, Benchmarking resolution enhancement performance. a-b**, Boxplots of SSIM (top) and RMSE (bottom) for FOCUS and nine competing methods, in scenarios where high-resolution (HR) ST (**a**) or only low-resolution (LR) ST are available (**b**). FOCUS consistently achieves the best performance. **c-d,** Scatter plots comparing gene-wise SSIM by FOCUS (x-axis) and iStar[13] (best-performing; y-axis) for mouse brain (**c**) and human breast cancer (**f**) on Xenium. Canonical tissue marker genes are highlighted in red, indicating that FOCUS more effectively recapitulates their spatial patterns than iStar. **e-f,** Representative spatial patterns of marker genes for mouse brain (*Snap25, Aldoc*; **e**) and human breast cancer (*GATA3, ERBB2*; **f**). Columns show the H&E image, LR ST, ground-truth HR ST, and ST generated by FOCUS, and Diff-ST[12] and iStar[13] (top two best-performing), where FOCUS-generated ST most matches the HR ST maps. **(g-h), Improved spatial domain characterization with enhanced resolution. g**, Quantitative comparisons of FOCUS-derived *versus* competing methods-derived spatial domains, using the Jaccard index, adjusted Rand index, and average surface distance, show that FOCUS most accurately recovers the true spatial organization. **h**, Illustration of spatial domains inferred from super-resolved ST by FOCUS, Diff-ST, and iStar, with H&E images shown as reference.

2.3 FOCUS enhances ST spatial resolution

By using high-resolution (HR) ST as the generation target and conditioning on H&E images with rich cellular morphology, FOCUS achieves resolution enhancement. We compared FOCUS with generic image enhancement (U-Net[36], Advanced U-Net[37], Nested U-Net[38], nnU-Net[39]) and ST-specific methods[2] (xFuse[40], TESLA[11], HSG[41], iStar[13], Diff-ST[12]) (Fig. 2). Performance was evaluated at a 10× scale-up[3], from 100 μm/pixel to single-cell resolution of 10μm/pixel, using root mean square error (RMSE) and structural similarity index measure (SSIM) to assess pixel-wise accuracy and structural preservation.

First, we benchmarked FOCUS on two HR platforms (VisiumHD [mouse kidney, embryo], and Xenium [human breast cancer, mouse brain]) using synthetic low-resolution (LR) ST (Fig. 2a). Performance is evaluated against native HR platforms as the ground truth. Across tissues and platforms, FOCUS consistently outperformed competing methods, reducing RMSE by at least 0.05 and increasing SSIM by at least 0.18 (both $P<0.001$).

Then, we utilized FOCUS to enhance native low-resolution (LR) platforms: Visium (probe) [mouse brain] and Spatial Transcriptomics [human breast cancer] (Fig. 2b). As HR ST is unavailable, following prior work[12,13], we downsampled the enhanced ST to LR and

[2] To ensure fairness, all methods are provided with matched H&E images and low-resolution ST.

[3] FOCUS can achieve arbitrary enlargement times. This study only evaluated FOCUS at 10x scale.

calculated SSIM and RMSE with native LR. FOCUS consistently performed the best across all comparisons, with SSIM gains of 0.29 and 0.28, and RMSE reductions of 0.09 and 0.06 (all $P < 0.001$) on Visium (probe) and Spatial Transcriptomics, respectively, highlighting its utility for real-world LR platforms.

Further, we assessed gene-wise spatial fidelity on Xenium for the mouse brain and human breast cancer (Fig. 2c-f). Per-gene SSIM scatter plots show that most genes have higher SSIM values by FOCUS compared to competing methods, including key markers (e.g., *Tubb3, Snap25, Gfap,* and *Aldoc* in mouse brain, *TPD52, GATA3, SERPINA3,* and *ERBB2* in human breast cancer, and *Umod*, *Cdh16*, *Sdhc*, *Igfbp7* and *Cd63* in mouse kidney) (Fig. 2c-d, Fig. S4). Example visualization further confirms that FOCUS provides sharper, anatomically coherent gene patterns than competing methods, reflecting its consistency with H&E structure (Fig. 2e-f).

Finally, we evaluated whether FOCUS-enhanced resolution improves downstream analysis sensitive to resolution. We focused on spatial domain characterization because low-resolution spots mix neighboring regions, blurring domain boundaries. Spatial domains inferred from FOCUS-reconstructed HR ST best matched domains from platform HR ST across tissues, with the highest Jaccard and adjusted Rand indices, and the lowest surface distance[4] (Fig. 2g-h), across both sequencing- (VisiumHD) and imaging-based (Xenium) platforms. This implies that FOCUS-enhanced resolution enables more accurate and robust delineation in the spatial domain.

[4] These three metrics are commonly used for evaluating spatial domain similarity.

Global Sensitivity enhancement for entire tissues

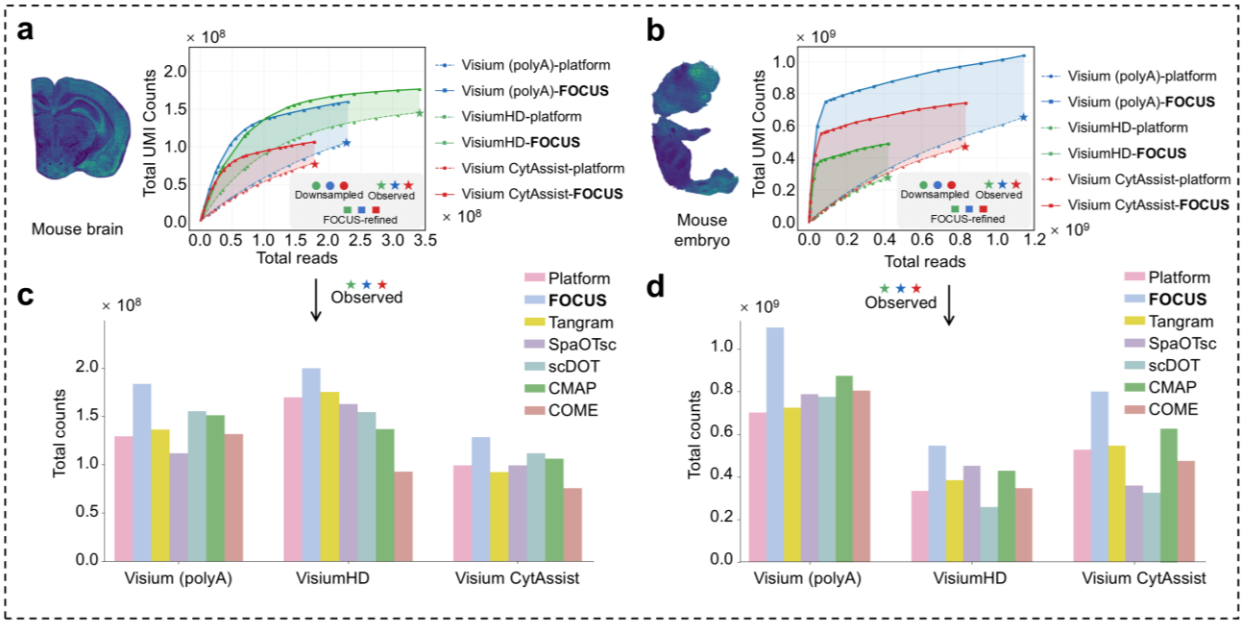

Sensitivity enhancement in known morphology

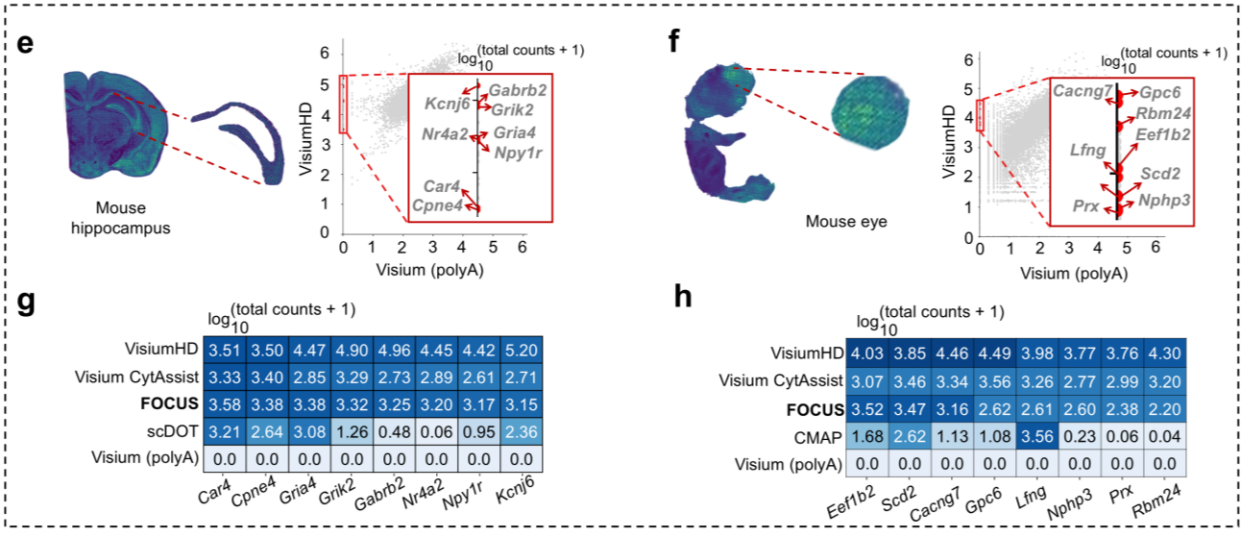

Validation of the added value of H&E for sensitivity beyond scRNA

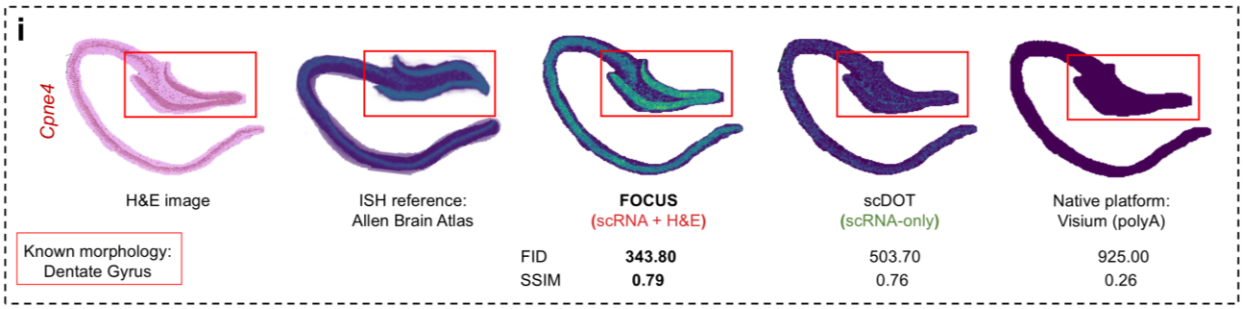

Fig. 3 | Validation of FOCUS in sensitivity enhancement. (**a-d**)**, Global sensitivity enhancement for entire tissues. a-b,** Comparison of FOCUS-enhanced with native platform-derived total counts, at both observed full set and downsampled sequencing depth (reads), on various platforms (Visium (polyA), VisiumHD, and Visium CytAssist) for mouse brain (**a**) and embryo (**b**). FOCUS increases sensitivity with higher total counts across platforms. **c-d,** At the observed depth, FOCUS outperforms scRNA-based competing methods in enhancing sensitivity, measured as higher total counts, for mouse brain (**c**) and embryo (**d**). (**e-h**)**, Sensitivity enhancement for regions of known morphology. e-f,** Total counts of detected genes are compared between Visium (polyA) (x-axis) and VisiumHD (y-axis) in the mouse hippocampus (**e**) and embryonic eye (**f**). Each dot represents a gene, shown in grey. Marker genes with high expression in VisiumHD but undetectable in Visium (polyA) are highlighted and labeled. **g-h,** Heatmaps showing $\log_{10}$-expression for genes not captured by Visium (polyA) and recovered by FOCUS, which are consistently captured by reference platforms (VisiumHD and Visium CytAssist) for mouse hippocampus (**g**) and embryonic eye (**h**). **i**, **Contribution of H&E for sensitivity beyond scRNA-seq reference.** Spatial expression of *Cpne4* along the dentate gyrus in mouse hippocampus, comparing native Visium (polyA), FOCUS and scDOT (using only scRNA-seq), with the paired H&E and *in situ* hybridization reference from the Allen Brain Atlas (ABA). Compared with scDOT, FOCUS further leverages H&E structural guidance and reconstructs the dentate gyrus architecture, achieving lower FID and higher SSIM relative to the ABA reference.

2.4 FOCUS improves ST sensitivity

By integrating scRNA-seq, spatial gene co-expression priors, and H&E guidance in the OT-based rectification module, FOCUS enhances ST sensitivity, especially for lowly expressed genes. Following prior works[3], we quantified sensitivity using total unique molecular identifier (UMI) counts, which represent the mRNA capture efficiency under fixed assay conditions and tissue area[2,3]. Additionally, we also evaluated recovery of poorly captured genes with high-sensitivity *in situ* hybridization (ISH) as ground truth. We benchmarked FOCUS under two scenarios as follows.

Global enhancement in the whole tissue

First, we validated FOCUS across the whole tissue using widely studied mouse brain and embryo, on the Visium (polyA), Visium CytAssist, and VisiumHD platforms. FOCUS increased total UMI counts under both the physically observed and downsampled[3] sequencing depth (reads) (Fig. 3a-d). For example, in the observed data, total counts increased from 1.08×10^8 to 1.61×10^8 ($P < 0.001$) for Visium (polyA) mouse brain, and from 2.87×10^8 to 4.95×10^8 ($P < 0.001$) for VisiumHD mouse embryo. Notably, FOCUS tended to yield larger sensitivity gains at lower depths (e.g., an 86% increase at 8.68×10^7

reads *versus* 35% at 1.77×10^8 reads for Visium CytAssist mouse brain) (Fig. 3a-b), highlighting its effectiveness in low-throughput settings.

For extensive benchmarking, we further compared FOCUS with five competing methods (Tangram, SpaOTsc, scDOT, CMAP, and COME) that leverage scRNA-seq to enhance sensitivity. At the observed sequencing depth, FOCUS achieved the highest total UMI counts among all competitors, consistently across the three platforms (Fig. 3c-d). Beyond the increase of total counts, FOCUS also preserved the overall expression patterns across the transcriptome, with high spatial Pearson correlation coefficients (PCC) between FOCUS and native platforms (e.g., 0.84, 0.92, and 0.83 on Visium (polyA), VisiumHD and Visium CytAssist for mouse brain), likely driven by incorporating spatial co-expression prios, consistently surpassing all competing methods (Extended Fig. 4).

Local enhancement in regions of known morphology

Further, we validated FOCUS in regions with distinct morphology, including the mouse hippocampus and embryonic eye (Fig. 3e-h). We first segmented the hippocampus and embryonic eye regions from the whole tissues. Through pairwise comparisons across platforms, we identified marker genes undetectable in Visium (polyA) but consistently expressed across reference platforms of VisiumHD and Visium CytAssist, e.g., *Car4, Cpne4, Gria4, Grik2, Gabrb2, Nr4a2, Npy1r,* and *Kcnj6* in the mouse hippocampus (Fig. 3e, Fig. S5a). FOCUS-restored expressions for Visium (polyA) were consistent with those of reference platforms, e.g., achieving a PCC of 0.75 (95% CI 0.72-0.79, $P<0.001$) with Visium CytAssist (Fig. 3g). Similar results were obtained in the embryonic eye (Fig. 3f, h, Fig. S5b), suggesting that FOCUS can enhance low-profiling sensitivity within defined local morphologies.

Validation of H&E morphology in sensitivity enhancement

Finally, to assess the contribution of H&E to sensitivity enhancement, we compared FOCUS with the best-performing competing method, scDOT, which uses only scRNA-seq. Analyses focused on the dentate gyrus region in the mouse hippocampus, a region with high-contrast tissue structure. FOCUS-enhanced ST better preserved dentate gyrus

structure, while also matching the Allen Brain Atlas *in situ* hybridization reference[45], assessed by Fréchet Inception Distance (FID) and SSIM (Fig. 3i). For *Cpne4*, a synaptic marker gene with clear expression in dentate gyrus[46], FOCUS achieved the lowest FID and highest SSIM (FID 343.80, SSIM 0.79), outperforming scDOT (FID 503.70, SSIM 0.76; $P < 0.001$), illustrating the added value of H&E guidance for sensitivity enhancement.

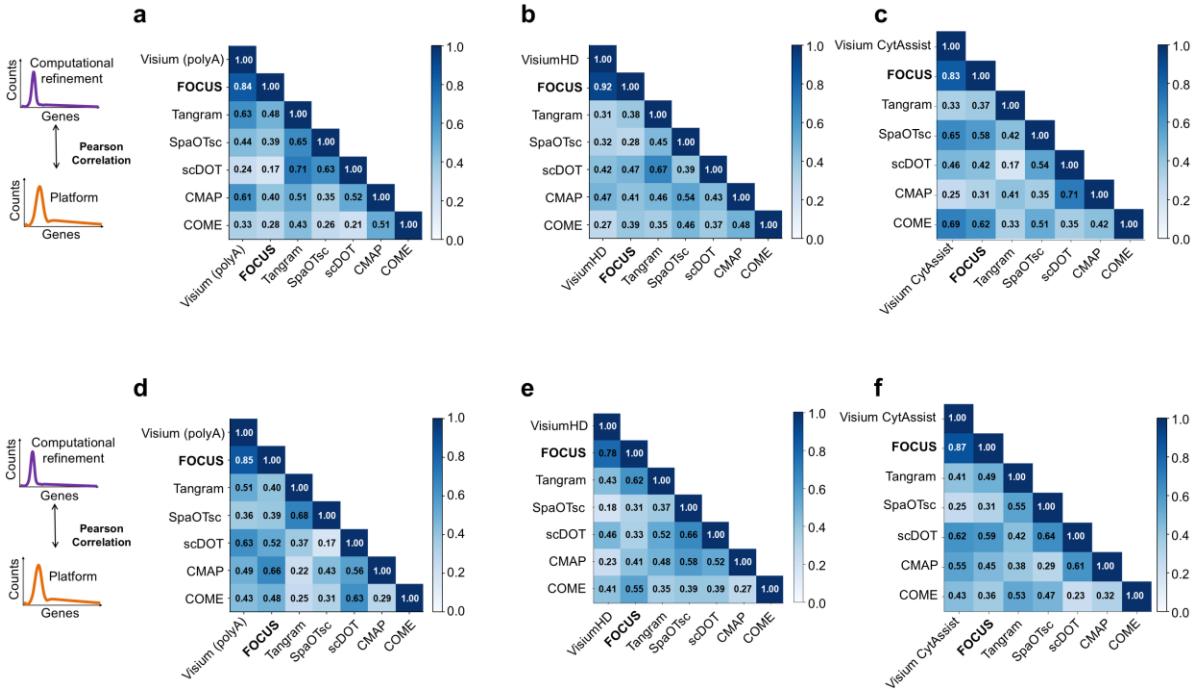

Extended Fig. 4 | FOCUS best preserves global expression patterns of platform-derived ST. Spatial PCC between native and FOCUS-enhanced ST are 0.83, 0.92, and 0.83 for mouse brain (**a**, Visium (polyA); **b**, VisiumHD; **c**, Visium CytAssist) and 0.85, 0.78, and 0.87 for mouse embryo (**d**, Visium (polyA); **e**, VisiumHD; **f**, Visium CytAssist), outperforming all competing methods and demonstrating robust cross-platform enhancement of sensitivity.

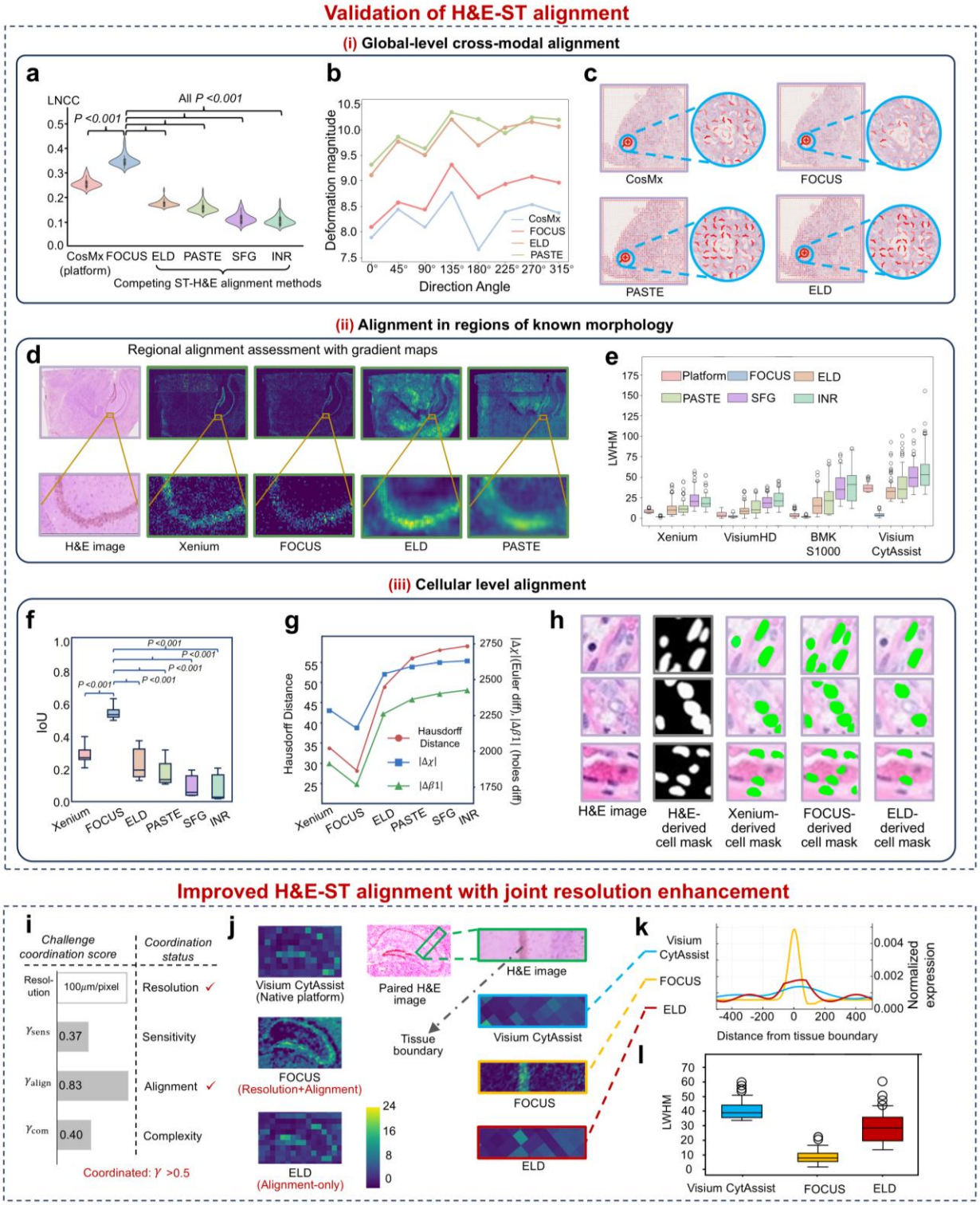

Fig. 4 | Evaluation of FOCUS in aligning ST with tissue structures. a-c, Global alignment. Overall alignment (quantified by LNCC; **a**) and deformation magnitudes across deformation directions (**b**). FOCUS consistently yields the highest LNCC and the lowest deformations, compared with the native CosMx platform and competing methods, indicating improved alignment with less warping. **c**, Illustration of deformation fields of CosMx, FOCUS, and competing

methods. **d-e,** Regional alignment with tissue structures. **d,** Gradient visualization of H&E and ST in the mouse hippocampus, with FOCUS best preserving the known laminar morphology. **e**, Left half-width at half-maximum[3] (LWHM) distribution across four platforms, where FOCUS consistently performs the best, indicating the sharpest and most localized gene expression. **f-h,** Cellular level alignment. Pixel-wise (**f**) and topological (**g**) discrepancies between H&E- and ST-derived cell masks. FOCUS yields the smallest differences, indicating its closest agreement in cellular morphology and tissue topology. **h,** Representative cellular patches with H&E and corresponding cell masks derived from the native platform, FOCUS, and compared methods. **(i-l)**, **Improved alignment with joint resolution enhancement, validated on Visium CytAssist mouse brain. i,** The challenge coordination score, which indicates the activation status of each challenge (Methods), shows co-occurrence of low resolution and poor alignment, indicating joint optimization in FOCUS. **j-l,** Spatial expression patterns in the mouse hippocampus for the native platform, FOCUS, and ELD (**j**), with alignment quality quantified by normalized expression (**k**) and LWHM (**l**). Compared with ELD, which optimizes alignment only, FOCUS-generated ST better aligns with tissue structures in H&E images, demonstrating the benefit of joint resolution enhancement for alignment.

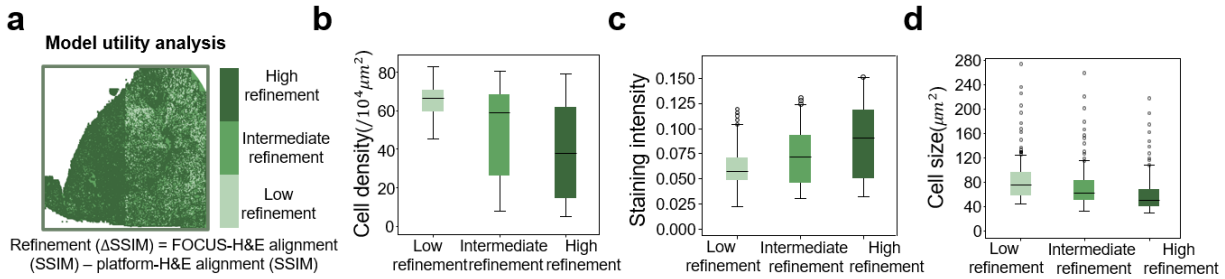

Extended Fig. 5 | Model utility analysis relating alignment enhancement (ΔSSIM) to histological features on CosMx. ΔSSIM denotes the increase in cross-modal SSIM of FOCUS-generated ST relative to the native platform. **a**, tissue map stratified into low, intermediate, and high ΔSSIM regions. **b-d**, distributions of cell density (**b**), staining intensity (**c**), and cell size (**d**) across these groups show that alignment enhancement is greatest in regions with stronger staining, lower cell density, and smaller cells, indicating that FOCUS most effectively corrects alignment in well-defined cellular structures.

2.5 FOCUS improves alignment with tissue structures

2.5.1 Standalone validation of alignment

FOCUS improves the alignment with tissue structures across platforms and spatial levels, enabled by its morphology-expression modulation module. We tested the accuracy at global (tissue deformation), regional (alignment in known morphology), and cellular (local, lateral mRNA diffusion) levels (Fig. 4). For comprehensive evaluation, we compared with state-of-the-art image registration methods adapted for alignment with tissue structures (PASTE[47], INR[48], SFG[49]), and ELD[50], specially designed for ST data.

Global validation on the whole tissue

First, we benchmarked FOCUS across whole tissues, using the human colon cancer (CosMx), human breast cancer (Xenium) and mouse brain (BMK S1000). We followed prior work[48,50] and used local normalized cross-correlation (LNCC) and SSIM to quantify structural consistency between H&E and ST gradient maps. On CosMx, FOCUS outperformed both the native platform and competing methods, achieving the best LNCC (0.352, 95%CI 0.332-0.376; P<0.001) and SSIM (0.386, 95%CI 0.347-0.420; P<0.001) (Fig. 4a, Fig. S6). Similar alignment gains were observed by FOCUS on human breast cancer (Xenium) and mouse brain (BMK S1000) (Fig. S7a, Fig. S8a-b), suggesting its effectiveness in aligning ST and H&E images.

For robustness validation, we then examined the deformation magnitude across different direction angles (from 0° to 315°) on both CosMx and Xenium. FOCUS produced the lowest H&E-ST deformation magnitudes across all angles, compared to both native platforms and competing methods (mean deformation magnitude: FOCUS 8.31 *versus* native platform 8.78, ELD 9.77, and PASTE 9.91 on CosMx; FOCUS 9.29 *versus* native platform 9.77, ELD 10.88, and PASTE 10.99 on Xenium) (Fig. 4b-c, Fig. S8c-d), indicating its robustness across local deformations.

We also evaluate FOCUS's alignment gains to different tissue contexts. We observe that regions with higher ΔSSIM (i.e., SSIM increase over the native platform) tended to show lower cell density (mean 63, 51, 39 cells per $10^4 \mu m^2$ for low-, intermediate-, and high ΔSSIM regions), higher staining intensity (mean 0.061, 0.072, and 0.095), and smaller cell sizes (mean 79, 68, 52 μm^2; Extended Fig. 5). These results demonstrate the performance of FOCUS is relatively stable, though tends to perform better in less complex tissue regions.

Regional validation in known morphology

We next evaluated lateral diffusion correction in selected anatomical structures, i.e., the mouse brain hippocampus. Two metrics were used: SSIM between H&E and ST gradient maps (Fig. S9), and the left-width at half-maximum[3] (LWHM) of expression peaks (Fig.

S10). For LWHM, we focused on histological regions where spatial expression should exhibit sharp contrast, with high expression in one subregion and minimal or no expression in the others. Across platforms, FOCUS consistently narrowed lateral spread and sharpened boundary transitions compared to native platforms, as reflected by LWHM (Xenium: FOCUS 5.21, native platform 9.78; VisiumHD: FOCUS 6.12, platform 3.73; BMK S1000: FOCUS 4.57, native platform 7.84; Visium CytAssist: FOCUS 6.68, platform 38.26), while also outperforming competing methods (Fig. 4d-e).

Cellular alignment validation

Furthermore, we assessed cellular-level alignment on human breast cancer patches (Xenium), as misalignment often occurs in complex tumor regions where lateral diffusion mixes signals between neighboring cells (Fig. 4f-h). FOCUS increased Intersection over Union (IoU) between cell masks derived from H&E and ST maps to 0.57 (95%CI 0.53-0.59; $P<0.001$), outperforming Xenium (0.28, 95%CI 0.26-0.29; $P<0.001$), and competing methods of ELD (0.24, 95%CI 0.21-0.29; $P<0.001$), PASTE (0.19, 95%CI 0.17-0.23; $P<0.001$), SFG (0.11, 95%CI 0.07-0.15; $P<0.001$), and INR (0.07, 95%CI 0.03-0.08; $P<0.001$) (Fig. 4f). In addition, FOCUS generated smallest geometric and topological discrepancies between H&E- and ST-derived cell masks, evaluated by Hausdorff distance (FOCUS 28 versus Xenium 34), Euler (FOCUS 2157 versus Xenium 2290) and Holes difference (FOCUS 1788 versus Xenium 1914) (Fig. 4g). Finally, example visualization confirmed that FOCUS-enhanced ST minimized directional offsets between predicted gene expression and H&E-derived cell boundaries (Fig. 4h).

2.5.2 Joint enhancement of spatial resolution and alignment

Finally, we evaluated joint enhancement of co-occurring challenges of spatial resolution and alignment, because LR ST blurs boundaries in ST, possibly hindering accurate alignment with tissue structures (Fig. 4i-l). The native LR Visium CytAssist mouse brain was used. The challenge-coordination score, computed from module-specific scaling coefficients in the cross-challenge coordination strategy and indicating whether each challenge is activated (activated if >0.5; Methods), confirmed that FOCUS jointly optimizes spatial resolution and alignment (Fig. 4i). Compared with the best-performing

competing method, ELD, which optimizes alignment only, FOCUS-generated ST aligned better with H&E (Fig. 4j), showing a sharper expression distribution ($P < 0.001$; Fig. 4k), and achieving a much lower average LWHM (8.5 *versus* 39.2 for ELD; $P < 0.001$; Fig. 4l). These results demonstrate the benefit of joint spatial resolution enhancement and alignment with tissue structures.

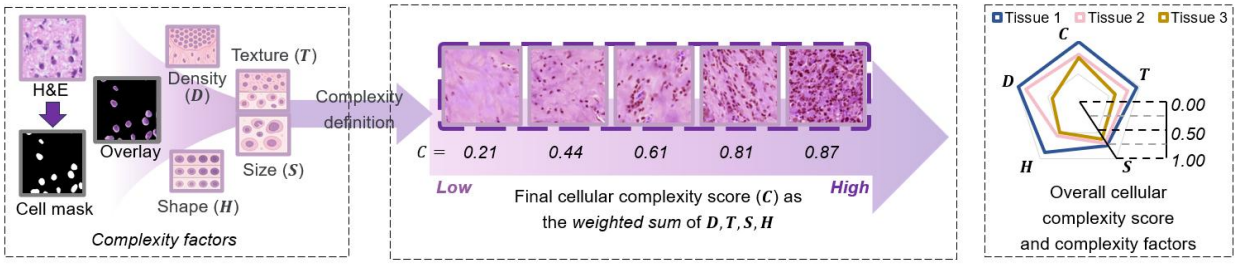

Extended Fig. 6 | Schematic definition of tissue complexity. For a given tissue patch, complexity is determined by cell density and heterogeneity (cell-type diversity), with the latter captured by variations in cell size, shape, and texture.

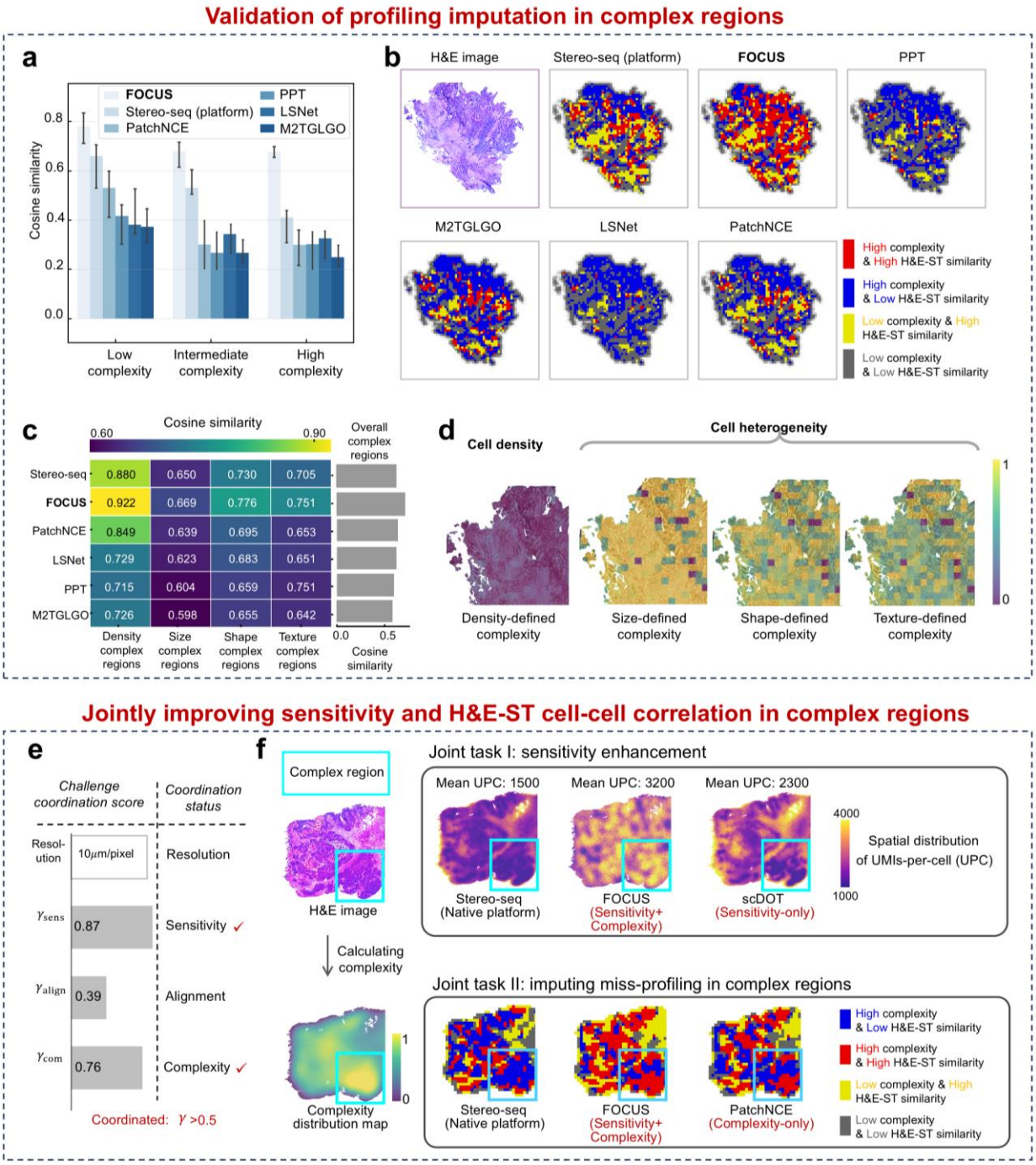

Fig. 5 | Enhancement of profiling precision in complex regions. a, Cosine similarity between cell-cell correlation matrices derived from H&E and ST (from the native Stereo-seq platform, FOCUS, and competing methods) across low-, intermediate-, and high-complexity regions. FOCUS achieves the greatest improvement in cosine similarity, especially in high-complexity regions. **b**, Spatial maps of complexity and H&E-ST feature consistency, with pixels classified by joint categories of complexity and feature consistency; FOCUS yields the largest extent of high-complexity regions with high H&E-ST feature consistency. **c-d**, Model robustness analysis. **c**, Cosine similarity (defined in **a**) in high-complexity regions *determined* by various factors of cell density, size, shape, texture and their combination (Methods). FOCUS

consistently maintains the highest similarity compared to the native platform and competing methods, demonstrating its robust profiling performance. **d** Illustration of the spatial distribution of factor-specific complexity in a human colon cancer tissue section on Stereo-seq. **(e-f)**, **Joint enhancement of challenges in sensitivity and complexity, tested on Stereo-seq ovarian cancer. e,** The challenge coordination score reveals co-occurring challenges of sensitivity and complexity for joint optimization in FOCUS. **f,** Left: H&E image with the corresponding complexity map, where low sensitivity (quantified by UMIs per cell) and poor H&E-ST feature consistency co-occur. Right: performance comparison with single-task baselines, i.e., scDOT for sensitivity and PatchNCE for complexity. FOCUS performs best on both tasks, demonstrating the benefit of joint optimization.

2.6 FOCUS balances profiling across tissue complexity

2.6.1 Standalone validation of complexity challenge

Guided by H&E-derived cell-cell correlations, FOCUS imputes miss-profiling in complex regions, thereby improving profiling balance across tissue complexity. We quantified the overall tissue complexity using hallmark histological features, including cell density and spatial variations in texture, size, and shape (Extended Fig. 6; Methods). We benchmarked FOCUS against M2TGLGO[51], designed for H&E-based ST generation and state-of-the-art image-to-image translation methods (ASP[52], PPT[53], and LSNet[54]) adapted for imputing miss-profiling in ST.

Benchmarking was conducted on Stereo-seq of human colon cancer, with pronounced heterogeneity in tissue complexity across tumor and infiltrative areas. We quantified the correction of mixing artifacts using the cosine similarity between H&E-derived and ST-derived cell-cell correlation matrices. FOCUS achieved the highest cosine similarity across areas of low (0.78, 95%CI 0.70-0.84; $P<0.001$), intermediate (0.66, 95%CI 0.62-0.71; $P<0.001$), and high complexity[5] (0.66, 95%CI 0.64-0.69; $P<0.001$; Fig.5a-b), outperforming both native platform and competing methods in ST-H&E concordance. Of note, FOCUS achieved the largest cosine similarity improvement in more complex areas prone to high mixing artifacts, with the increase of 0.25 in high-complexity *versus* 0.13 and 0.14 in low- and intermediate-complexity (Fig. 5a). We also observed similar improvement in the mouse brain on Xenium (Fig. S11a), indicating broad utility on normal

[5] Defined by dividing the complexity score into three equal tertiles (low, intermediate, high).

tissues. These results suggest the value of our ST-H&E constraining strategy, which leverages ST-H&E cell-cell correlations to improve profiling precision in complex tissues.

To further assess *robustness*, FOCUS was evaluated across variously defined levels of complexity based on factors such as cell density, cell size, shape, and texture. For high-complexity regions defined by each factor, FOCUS consistently achieved the highest cosine similarity on both Stereo-seq human colon cancer (density 0.922, size 0.669, shape 0.776, texture 0.751) and Xenium mouse brain (density 0.841, size 0.815, shape 0.823, texture 0.838) (Fig. 5c-d; Fig. S12), outperforming both native platforms and competing methods in ST-H&E concordance, indicating robust performance.

2.6.2 Joint validation of sensitivity and complexity challenges

Finally, we validated FOCUS in the context of co-occurring challenges of sensitivity and complexity, as high tissue complexity, e.g., high cell density, limits the capture of individual molecules per cell (e.g., UMIs), thereby reducing sensitivity. We used Stereo-seq ovarian cancer data, which contain both low-sensitivity[3] and complex tumor regions (Fig. 5e-f). As shown in Fig. 5f, high-complexity areas exhibit fewer UMIs per cell and low H&E-ST feature consistency. The challenge-coordination score confirmed that FOCUS evaluated and jointly mitigated both challenges (Fig. 5e). Compared with the best single-task baselines, i.e., scDOT for sensitivity and PatchNCE for complexity, FOCUS achieved a higher per-cell UMI count (3,200 *versus* 2,300 for scDOT; $P < 0.001$) and a larger area with high H&E-ST similarity in complex regions (82% *versus* 53% for PatchNCE; $P < 0.001$) (Fig. 5f). These results demonstrate the benefit of joint optimization across sensitivity and complexity via the challenge-coordinated strategy.

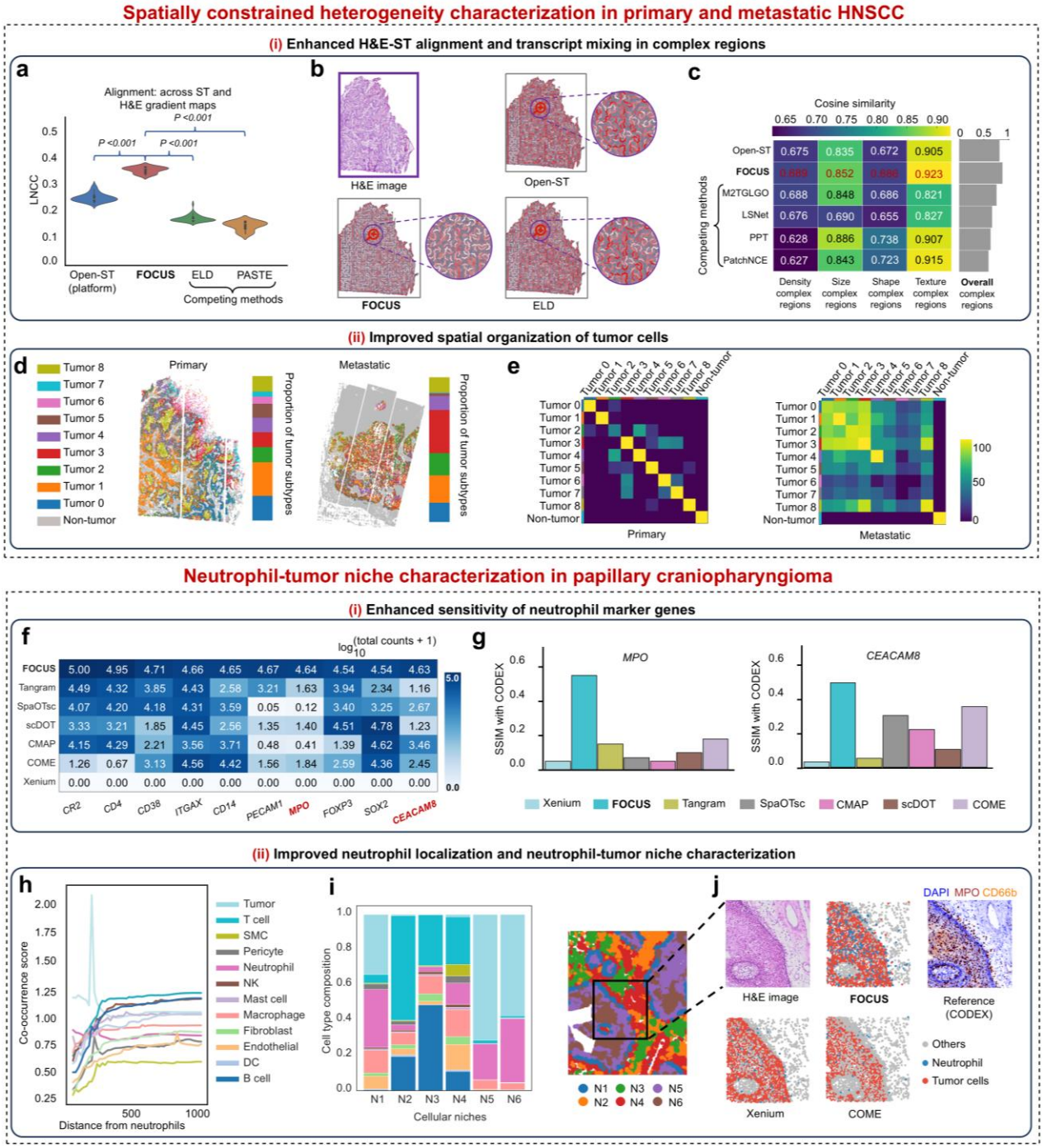

Fig. 6 | Real-world utility validation of FOCUS. (a-e) Spatially constrained heterogeneity characterization in primary and metastatic HNSCC on Open-ST. a-c, Enhanced alignment with tissue structures and feature consistency in complex regions. **a**, Alignment quantified by LNCC, comparing FOCUS with Open-ST and competing methods. **b**, Illustration of deformation fields, indicating improved alignment with less warping in FOCUS. **c**, Cosine similarity between H&E- and ST-derived cell-cell correlation matrices in complex regions *determined* by various factors of cell density, size, shape, texture, and their combination (Methods). **d-e,** Improved spatial organization of tumor cells. **d**,

Spatial maps of tumor transcriptomic states (T0-T8) from FOCUS-enhanced ST in primary and metastatic HNSCC. The primary tumor shows large, coherent domains, whereas the metastasis displays intermixed patterns. **e**, Heatmaps of neighborhood enrichment scores among tumor states (defined in **d**) computed from FOCUS-enhanced ST for primary (left) and metastatic (right) tumors. The primary tumor displays strong state-specific neighborhood enrichment, whereas the metastatic tumor exhibits more diffuse enrichment patterns, consistent with increased spatial intermixing. **(f-j) Neutrophil-tumor niche characterization for PCP on Xenium. f-g,** Sensitivity enhancement. **f,** Heatmap of $\log_{10}$-expression for genes poorly detected by Xenium, including neutrophil markers *MPO* and *CEACAM8*. FOCUS recovers these genes and shows stronger expression than competing methods. **g,** SSIM between ST and CODEX for neutrophil marker genes (*MPO* (left) and *CEACAM8* (right)*)*, showing higher similarity for FOCUS-enhanced ST than ST from Xenium platform and competing methods. **h-j,** Improved neutrophil-tumor niche characterization. **h**, Co-occurrence scores between neutrophils and other cell types for FOCUS-enhanced ST. Tumor cells are the dominant neighbors of neutrophils, revealing pronounced neutrophil-tumor niches. **i**, Neutrophil-centered cellular niches (N1-N6) obtained by ST clustering. All niches enriched with tumor cells (N1, N5, and N6) consistently confirm the neutrophil-tumor co-localization patterns inferred in **h. j**. Example region containing all three tumor-enriched niches identified in **i**, showing the neutrophil-tumor niche with CODEX reference.

2.7 FOCUS uncovers spatially constrained heterogeneity in primary and metastatic HNSCC on Open-ST

Beyond benchmarking, we applied FOCUS in an unseen ST platform, Open-ST, to evaluate its cross-platform generalization. Open-ST is a recently published high-resolution platform that profiles consecutive sections. Despite strengths, Open-ST has reported anisotropic lateral diffusion and inaccurate cell localization[55], which could lead to misalignment with tissue structures and transcript mixing in complex regions. We thereby applied FOCUS to enhance Open-ST data, enabling clearer characterization of the spatially constrained transcriptomic heterogeneity in primary HNSCC and its metastatic lymph node (Fig. 6a-e), where subtle cell-cell co-localizations are critical for interpreting metastasis.

First, FOCUS jointly improved alignment with tissue structures and profiling precision in complex regions compared with the native platform and competing methods (Fig. 6a-c, Figs. S13-14). Using the enhanced ST, we clustered ~45,000 tumor cells from primary and metastatic lesions into nine transcriptomic states (T0-T8). In the primary tumor, these states formed spatially coherent domains, whereas in the metastatic lymph node they were highly intermixed (Fig. 6d), as further supported by the neighborhood enrichment analysis (Fig. 6e), consistent with prior findings that metastasis displays disrupted spatial

architecture[68]. This spatial difference was relatively small in the native platform (neighbor-mixing score: 0.22 for primary *versus* 0.29 for metastasis) but more pronounced with FOCUS-enhanced ST (0.18 *versus* 0.46) (Fig. S15). These results indicate that FOCUS-enhanced ST effectively captures the increased spatial disruption in metastasis, likely through FOCUS's improved alignment and profiling precision in complex regions.

2.8 FOCUS elucidates neutrophil-tumor niche characterization in papillary craniopharyngioma

Further, we applied FOCUS in an unseen tissue context of PCP to validate its real-world utility. PCP is a rare suprasellar tumor that frequently exhibits a neutrophil-rich inflammatory microenvironment. However, activated neutrophils exhibit transient transcriptional activity and a short lifespan, making mRNAs unstable and less sensitive to capture. Therefore, we collected real-world patient samples (n=3[6]) from PCP and utilized FOCUS to enhance ST for characterizing neutrophil-tumor niches.

To characterize neutrophil-tumor niches, we first used FOCUS to enhance the sensitivity of lowly expressed genes, including neutrophil markers such as *MPO* and *CEACAM8,* by fine-tuning FOCUS on the PCP dataset (Xenium) (Fig. 6f-g). Of note, we use high-sensitivity spatial proteomics (CODEX[59], profiled using adjacent tissue sections of those for Xenium) as reference, shown in Fig. S16. FOCUS markedly increased the sensitivity (total counts) over the native platform and competing methods (Fig. 6f). FOCUS-enhanced ST also showed much higher structural concordance with CODEX (protein-level validation) over the native platform, measured by SSIM (*MPO*: 0.58 *versus* 0.05; *CEACAM8*: 0.51 *versus* 0.03, both $P<0.001$) (Fig. 6g, Fig. S17).

Based on the FOCUS-enhanced ST, neutrophil localization was improved, revealing co-localized neutrophils and tumor cells. The distance-based cell co-occurrence analysis showed that tumor cells were the dominant neighbors of neutrophils (Fig. 6h). This pattern was particularly evident in three niches enriched with tumor cells (Niche 1, 5, and 6; Fig. 6i), identified by ST spatial clustering analysis. In an example region containing all three

[6] 3 patients (1 for fine-tuning and 2 for testing) with 24 paired ST-H&E images in total.

niches, FOCUS-enhanced ST revealed dense neutrophil clusters and tumor nests that were largely missed by the native platform (evidenced by CODEX data in Fig. 6j), consistent with previous findings of enriched neutrophils in intratumoral parenchyma of PCP[60]. These results indicate the usefulness of FOCUS-enhanced ST in discovering neutrophil-tumor niches, informing disease courses and treatment responses[61].

Discussion[62–64]

FOCUS is a diffusion-based foundational generative model that jointly mitigates four coupled ST challenges, including spatial resolution, sensitivity to low expression, alignment with tissue structures and profiling balance across tissue complexity. Its performance rests mainly on three key aspects: (i) integration of multiple ST-complement modalities, (ii) coordinated interaction across challenges, and (iii) cross-platform foundational training.

First, inspired by recent advances of multimodal learning[62–64], FOCUS exploits complementary multimodal information within a modular architecture to jointly address multiple ST challenges. It uses scRNA-seq references, spatial co-expression, and H&E-gradient guidance to boost sensitivity; H&E-derived cellular morphology and H&E-ST spatial concordance to enhance resolution and alignment; and H&E-guided cell-cell correlation constraints to reduce signal mixing in complex regions. **Second**, a cross-challenge coordination strategy targets defects that tend to co-occur. For instance, misalignment with tissue structures often arises in regions of high tissue complexity, such as cancerous areas. Additionally, the coordination design also enables flexible module combinations for different real-world scenarios. **Finally**, FOCUS builds on large-scale pretrained H&E and ST encoders[23,24] that capture rich cellular morphology and spatial expression patterns. Further, FOCUS was jointly trained across 10 imaging- and sequencing-based platforms, leveraging their complementary strengths to enhance model robustness and generalizability.

Computational methods have been proposed for individual challenges. Representative spatial **resolution** enhancement approaches[11,12,65], e.g., iStar[13] and TESLA[11], improve spatial detail in ST by utilizing cellular morphology from paired H&E images, while **sensitivity** can be increased by integrating ST with scRNA-seq references, as in Tangram[4] and CMAP[66]. In parallel, methods such as ELD[50] aim to improve **alignment** with tissue structures by associating H&E texture features with ST gene patterns, and a few ST-decomposition methods, e.g., RCTD[10], have also been proposed to mitigate the signal mixing in **complex** regions. **Collectively**, most challenge-tailored methods ignore

the coupling of these challenges, the complementarity of multiple modalities, and the benefit of tackling them within a single framework. Our results demonstrate the state-of-the-art performance of FOCUS on both individual and coupled challenges across ten platforms, improving both native platforms and challenge-specific baselines.

In parallel, recent advances in foundational generative foundational models[19,20] have shown strong generative capabilities across natural image and text modalities, driven by large-scale pretraining and modular architectures that learn broadly robust representations. As a result, they often transfer effectively to new tasks and domains with minimal task-specific supervision, enabling rapid adaptation via prompting or lightweight fine-tuning, as shown by the performance of FOCUS across multiple enhancement tasks across different platforms. Compared to generic foundational models (Supplementary section 4), FOCUS achieves better performance on ST-specific tasks, leveraging the advantages of multimodal data and its ST-specific modular design.

We fine-tuned FOCUS on unseen platform or tissue context to assess real-world utility: **(i)** for primary and metastatic HNSCC on Open-ST, FOCUS rectified misalignment and transcript mixing, uncovering spatially heterogeneous neighborhood patterns across primary and metastatic sites; **(ii)** for PCP on Xenium, FOCUS recovered spatial patterns of neutrophil markers and characterized tumor-neutrophil niches that was largely missed by the native platform. Together, these examples support the real-world utility of FOCUS.

In summary, to our knowledge, FOCUS is the first computational method for jointly mitigating multiple ST challenges. We believe FOCUS will serve as a useful tool for enhancing ST on current or future platforms. There are also multiple avenues of possible extensions for FOCUS. One is to extend ST to spatial multi-omics, including proteomics and epigenomics, for systematic evaluation of current experiment-based spatial multi-omics technologies while tailoring computational models accordingly. We also aim to scale FOCUS-enhanced ST for the discovery of disease mechanisms and to advance clinical translation by linking discovered spatial patterns to clinical decision-making.

Reference

1. Systematic benchmarking of high-throughput subcellular spatial transcriptomics platforms across human tumors | Nature Communications. https://www.nature.com/articles/s41467-025-64292-3.
2. Wang, H. *et al.* Systematic benchmarking of imaging spatial transcriptomics platforms in FFPE tissues. *bioRxiv* 2023.12.07.570603 (2023) doi:10.1101/2023.12.07.570603.
3. You, Y. *et al.* Systematic comparison of sequencing-based spatial transcriptomic methods. *Nat. Methods* **21**, 1743–1754 (2024).
4. Biancalani, T. *et al.* Deep learning and alignment of spatially resolved single-cell transcriptomes with Tangram. *Nat. Methods* **18**, 1352–1362 (2021).
5. Cao, J. *et al.* Decoder-FFPE-seq enables sensitive, genome-wide spatial transcriptomics of archival tissues at single-cell resolution. 2025.09.12.675967 Preprint at https://doi.org/10.1101/2025.09.12.675967 (2025).
6. Wirth, J. *et al.* Spatial transcriptomics using multiplexed deterministic barcoding in tissue. *Nat. Commun.* **14**, 1523 (2023).
7. Ren, J. *et al.* Spatiotemporally resolved transcriptomics reveals the subcellular RNA kinetic landscape. *Nat. Methods* **20**, 695–705 (2023).
8. Williams, C. G., Lee, H. J., Asatsuma, T., Vento-Tormo, R. & Haque, A. An introduction to spatial transcriptomics for biomedical research. *Genome Med.* **14**, 68 (2022).
9. Kennedy-Darling, J. *et al.* Chapter 4 - Highly multiplexed spatial protein data using CODEX technology. in *Revealing Uncharted Biology With Single Cell Multiplex Proteomic Technologies* (ed. Fantl, W. J.) 93–118 (Academic Press, 2024). doi:10.1016/B978-0-12-822209-6.00001-1.
10. Cable, D. M. *et al.* Robust decomposition of cell type mixtures in spatial transcriptomics. *Nat. Biotechnol.* **40**, 517–526 (2022).
11. Hu, J. *et al.* Deciphering tumor ecosystems at super resolution from spatial transcriptomics with TESLA. *Cell Syst.* **14**, 404-417.e4 (2023).
12. Wang, X., Huang, X., Price, S. & Li, C. Cross-Modal Diffusion Modelling for Super-Resolved Spatial Transcriptomics. in *Medical Image Computing and Computer Assisted Intervention – MICCAI 2024* (eds Linguraru, M. G. et al.) 98–108 (Springer Nature Switzerland, Cham, 2024). doi:10.1007/978-3-031-72384-1_10.
13. Zhang, D. *et al.* Inferring super-resolution tissue architecture by integrating spatial transcriptomics with histology. *Nat. Biotechnol.* **42**, 1372–1377 (2024).
14. Zhang, P. *et al.* Thor: a platform for cell-level investigation of spatial transcriptomics and histology. *Nat. Commun.* **16**, 7178 (2025).
15. Huang, J. *et al.* Bridging cell morphological behaviors and molecular dynamics in multi-modal spatial omics with MorphLink. *Nat. Commun.* **16**, 5878 (2025).
16. Lin, Y. *et al.* ST-Align: A Multimodal Foundation Model for Image-Gene Alignment in Spatial Transcriptomics. Preprint at https://doi.org/10.48550/arXiv.2411.16793 (2024).
17. Sun, E. D., Ma, R., Navarro Negredo, P., Brunet, A. & Zou, J. TISSUE: uncertainty-calibrated prediction of single-cell spatial transcriptomics improves downstream analyses. *Nat. Methods* **21**, 444–454 (2024).
18. Vahid, M. R. *et al.* High-resolution alignment of single-cell and spatial transcriptomes with CytoSPACE. *Nat. Biotechnol.* **41**, 1543–1548 (2023).
19. Rombach, R., Blattmann, A., Lorenz, D., Esser, P. & Ommer, B. High-Resolution Image Synthesis With Latent Diffusion Models. in 10684–10695 (2022).
20. Podell, D. *et al.* SDXL: Improving Latent Diffusion Models for High-Resolution Image Synthesis. in (2023).
21. Wang, X., Price, S. & Li, C. C3-Diff: Super-resolving Spatial Transcriptomics via Cross-modal Cross-content Contrastive Diffusion Modelling. Preprint at https://doi.org/10.48550/arXiv.2511.05571 (2025).
22. Liu, A., Wang, X., Cai, J. & Li, C. Score-Based Diffusion Model for Unpaired Virtual Histology Staining. in *Computational Mathematics Modeling in Cancer Analysis* (eds Li, C., Qin, W., Wu, J. & Zaki, N.) 30–39 (Springer Nature Switzerland, Cham, 2026). doi:10.1007/978-3-032-06624-4_4.
23. Xu, H. *et al.* A whole-slide foundation model for digital pathology from real-world data. *Nature* **630**, 181–188 (2024).
24. Wang, C. *et al.* scGPT-spatial: Continual Pretraining of Single-Cell Foundation Model for Spatial Transcriptomics. 2025.02.05.636714 Preprint at https://doi.org/10.1101/2025.02.05.636714 (2025).
25. Schott, M. *et al.* Open-ST: High-resolution spatial transcriptomics in 3D. *Cell* **187**, 3953-3972.e26 (2024).
26. Yang, L. *et al.* Diffusion Models: A Comprehensive Survey of Methods and Applications. *ACM Comput Surv* **56**, 105:1-105:39 (2023).
27. Ronneberger, O., Fischer, P. & Brox, T. U-Net: Convolutional Networks for Biomedical Image Segmentation. in *Medical Image Computing and Computer-Assisted Intervention – MICCAI 2015* (eds Navab, N., Hornegger, J., Wells, W. M. & Frangi, A. F.) 234–241 (Springer International Publishing, Cham, 2015). doi:10.1007/978-3-319-24574-4_28.

28. Ståhl, P. L. *et al.* Visualization and analysis of gene expression in tissue sections by spatial transcriptomics. *Science* **353**, 78–82 (2016).
29. Visium CytAssist Spatial Gene Expression Reagent Kits User Guide | Official 10x Genomics Support. *10x Genomics* https://www.10xgenomics.com/support/cytassist-spatial-gene-expression/documentation/steps/library-construction/visium-cyt-assist-spatial-gene-expression-reagent-kits-for-ffpe.
30. Oliveira, M. F. de *et al.* High-definition spatial transcriptomic profiling of immune cell populations in colorectal cancer. *Nat. Genet.* **57**, 1512–1523 (2025).
31. Ståhl, P. L. *et al.* Visualization and analysis of gene expression in tissue sections by spatial transcriptomics. *Science* **353**, 78–82 (2016).
32. Chen, A. *et al.* Spatiotemporal transcriptomic atlas of mouse organogenesis using DNA nanoball-patterned arrays. *Cell* **185**, 1777-1792.e21 (2022).
33. gd-admin. BMKMANU S1000 Spatial Transcriptome. *https://www.bmkgene.com/* https://bmkgene.com:443/bmkmanu-s1000-spatial-transcriptome-product/.
34. Xenium In Situ Platform. *10x Genomics* https://www.10xgenomics.com/platforms/xenium (2024).
35. He, S. *et al.* High-plex imaging of RNA and proteins at subcellular resolution in fixed tissue by spatial molecular imaging. *Nat. Biotechnol.* **40**, 1794–1806 (2022).
36. Ronneberger, O., Fischer, P. & Brox, T. U-Net: Convolutional Networks for Biomedical Image Segmentation. in *Medical Image Computing and Computer-Assisted Intervention – MICCAI 2015* (eds Navab, N., Hornegger, J., Wells, W. M. & Frangi, A. F.) 234–241 (Springer International Publishing, Cham, 2015). doi:10.1007/978-3-319-24574-4_28.
37. Oktay, O. *et al.* Attention U-Net: Learning Where to Look for the Pancreas. Preprint at https://doi.org/10.48550/arXiv.1804.03999 (2018).
38. Zhou, Z., Rahman Siddiquee, M. M., Tajbakhsh, N. & Liang, J. UNet++: A Nested U-Net Architecture for Medical Image Segmentation. in *Deep Learning in Medical Image Analysis and Multimodal Learning for Clinical Decision Support* (eds Stoyanov, D. et al.) 3–11 (Springer International Publishing, Cham, 2018). doi:10.1007/978-3-030-00889-5_1.
39. Isensee, F., Jaeger, P. F., Kohl, S. A. A., Petersen, J. & Maier-Hein, K. H. nnU-Net: a self-configuring method for deep learning-based biomedical image segmentation. *Nat. Methods* **18**, 203–211 (2021).
40. Bergenstråhle, L. *et al.* Super-resolved spatial transcriptomics by deep data fusion. *Nat. Biotechnol.* **40**, 476–479 (2022).
41. Pang, M., Su, K. & Li, M. Leveraging information in spatial transcriptomics to predict super-resolution gene expression from histology images in tumors. 2021.11.28.470212 Preprint at https://doi.org/10.1101/2021.11.28.470212 (2021).
42. Cang, Z. & Nie, Q. Inferring spatial and signaling relationships between cells from single cell transcriptomic data. *Nat. Commun.* **11**, 2084 (2020).
43. Nguyen, N. D. *et al.* scDOT: optimal transport for mapping senescent cells in spatial transcriptomics. *Genome Biol.* **25**, 288 (2024).
44. Wei, X. *et al.* COME: contrastive mapping learning for spatial reconstruction of single-cell RNA sequencing data. *Bioinformatics* **41**, btaf083 (2025).
45. Lein, E. S. *et al.* Genome-wide atlas of gene expression in the adult mouse brain. *Nature* **445**, 168–176 (2007).
46. von Ziegler, L. M., Selevsek, N., Tweedie-Cullen, R. Y., Kremer, E. & Mansuy, I. M. Subregion-Specific Proteomic Signature in the Hippocampus for Recognition Processes in Adult Mice. *Cell Rep.* **22**, 3362–3374 (2018).
47. Zeira, R., Land, M., Strzalkowski, A. & Raphael, B. J. Alignment and integration of spatial transcriptomics data. *Nat. Methods* **19**, 567–575 (2022).
48. Wolterink, J. M., Zwienenberg, J. C. & Brune, C. Implicit Neural Representations for Deformable Image Registration. in *Proceedings of The 5th International Conference on Medical Imaging with Deep Learning* 1349–1359 (PMLR, 2022).
49. Ge, L., Wei, X., Hao, Y., Luo, J. & Xu, Y. Unsupervised Histological Image Registration Using Structural Feature Guided Convolutional Neural Network. *IEEE Trans. Med. Imaging* **41**, 2414–2431 (2022).
50. Ekvall, M. *et al.* Spatial landmark detection and tissue registration with deep learning. *Nat. Methods* **21**, 673–679 (2024).
51. Shi, H., Chi, C., Wan, P., Zhang, D. & Shao, W. Multi-modal Topology-embedded Graph Learning for Spatially Resolved Genes Prediction from Pathology Images with Prior Gene Similarity Information. in *2025 IEEE/CVF Conference on Computer Vision and Pattern Recognition (CVPR)* 20810–20819 (2025). doi:10.1109/CVPR52734.2025.01938.
52. Li, F., Hu, Z., Chen, W. & Kak, A. Adaptive Supervised PatchNCE Loss for Learning H&E-to-IHC Stain Translation with Inconsistent Groundtruth Image Pairs. in *Medical Image Computing and Computer Assisted Intervention – MICCAI 2023* (eds Greenspan, H. et al.) 632–641 (Springer Nature Switzerland, Cham, 2023). doi:10.1007/978-3-031-43987-2_61.
53. Zhang, W. *et al.* High-Resolution Medical Image Translation via Patch Alignment-Based Bidirectional Contrastive Learning. in *Medical Image Computing and Computer Assisted Intervention – MICCAI 2024* (eds Linguraru, M. G. et al.) 178–188 (Springer Nature Switzerland, Cham, 2024). doi:10.1007/978-3-031-72083-3_17.

54. Wang, A., Chen, H., Lin, Z., Han, J. & Ding, G. LSNet: See Large, Focus Small. in *2025 IEEE/CVF Conference on Computer Vision and Pattern Recognition (CVPR)* 9718–9729 (2025). doi:10.1109/CVPR52734.2025.00908.
55. Schott, M. *et al.* Open-ST: High-resolution spatial transcriptomics in 3D. *Cell* **187**, 3953-3972.e26 (2024).
56. Karimi, E. *et al.* Single-cell spatial immune landscapes of primary and metastatic brain tumours. *Nature* **614**, 555–563 (2023).
57. Xu, K. *et al.* Microenvironment components and spatially resolved single-cell transcriptome atlas of breast cancer metastatic axillary lymph nodes. *Acta Biochim. Biophys. Sin.* **54**, 1336–1348 (2022).
58. Zhang, F. *et al.* Neutrophil diversity and function in health and disease. *Signal Transduct. Target. Ther.* **9**, 343 (2024).
59. Goltsev, Y. *et al.* Deep Profiling of Mouse Splenic Architecture with CODEX Multiplexed Imaging. *Cell* **174**, 968-981.e15 (2018).
60. Luo, N. *et al.* Comparative analysis of clinical features, methylation and immune microenvironment in pediatric and adult papillary craniopharyngiomas: results from a multicenter study. *Sci. Rep.* **15**, 27422 (2025).
61. Jia, Y. *et al.* Immune infiltration in aggressive papillary craniopharyngioma: High infiltration but low action. *Front. Immunol.* **13**, (2022).
62. Li, C. *et al.* Decoding the Interdependence of Multiparametric Magnetic Resonance Imaging to Reveal Patient Subgroups Correlated with Survivals. *Neoplasia* **21**, 442–449 (2019).
63. Zhang, Y., Wang, X., Meng, F., Tang, J. & Li, C. Knowledge-Driven Subspace Fusion and Gradient Coordination for Multi-modal Learning. in *Medical Image Computing and Computer Assisted Intervention – MICCAI 2024* (eds Linguraru, M. G. et al.) 263–273 (Springer Nature Switzerland, Cham, 2024). doi:10.1007/978-3-031-72083-3_25.
64. Que, N., Wang, X., Chen, J., Jiang, Y. & Li, C. Adaptive Spatial Transcriptomics Interpolation via Cross-modal Cross-slice Modeling. in *Medical Image Computing and Computer Assisted Intervention – MICCAI 2025* (eds Gee, J. C. et al.) 45–54 (Springer Nature Switzerland, Cham, 2026). doi:10.1007/978-3-032-04927-8_5.
65. Zhang, D. *et al.* Inferring super-resolution tissue architecture by integrating spatial transcriptomics with histology. *Nat. Biotechnol.* **42**, 1372–1377 (2024).
66. Ke, J. *et al.* High-resolution mapping of single cells in spatial context. *Nat. Commun.* **16**, 6533 (2025).
67. Zhang, P. *et al.* Thor: a platform for cell-level investigation of spatial transcriptomics and histology. *Nat. Commun.* **16**, 7178 (2025).
68. Kleshchevnikov, V. *et al.* Cell2location maps fine-grained cell types in spatial transcriptomics. *Nat. Biotechnol.* **40**, 661–671 (2022).
69. Long, Y. *et al.* Deciphering spatial domains from spatial multi-omics with SpatialGlue. *Nat. Methods* **21**, 1658–1667 (2024).
70. Weigert, M. & Schmidt, U. Nuclei Instance Segmentation and Classification in Histopathology Images with Stardist. in *2022 IEEE International Symposium on Biomedical Imaging Challenges (ISBIC)* 1–4 (2022). doi:10.1109/ISBIC56247.2022.9854534.
71. Redmon, J., Divvala, S., Girshick, R. & Farhadi, A. You Only Look Once: Unified, Real-Time Object Detection. Preprint at https://doi.org/10.48550/arXiv.1506.02640 (2016).
72. Wolf, F. A., Angerer, P. & Theis, F. J. SCANPY: large-scale single-cell gene expression data analysis. *Genome Biol.* **19**, 15 (2018).
73. Lee, J. *et al.* BioBERT: a pre-trained biomedical language representation model for biomedical text mining. *Bioinformatics* **36**, 1234–1240 (2020).
74. Sinkhorn, R. A Relationship Between Arbitrary Positive Matrices and Doubly Stochastic Matrices. *Ann. Math. Stat.* **35**, 876–879 (1964).
75. Chen, A. *et al.* Spatiotemporal transcriptomic atlas of mouse organogenesis using DNA nanoball-patterned arrays. *Cell* **185**, 1777-1792.e21 (2022).
76. Loshchilov, I. & Hutter, F. Decoupled Weight Decay Regularization. in (2018).
77. Dhariwal, P. & Nichol, A. Diffusion Models Beat GANs on Image Synthesis. in *Advances in Neural Information Processing Systems* vol. 34 8780–8794 (Curran Associates, Inc., 2021).
78. Palla, G. *et al.* Squidpy: a scalable framework for spatial omics analysis. *Nat. Methods* **19**, 171–178 (2022).
79. Nirmal, A. J. & Sorger, P. K. SCIMAP: A Python Toolkit for Integrated Spatial Analysis of Multiplexed Imaging Data. *J. Open Source Softw.* **9**, 6604 (2024).

Methods

1. Multimodal data processing

ST pre-processing

To preprocess the ST data from native platforms, we followed prior work[69] and filtered pixels that expressed fewer than 2% of the total genes and genes that expressed fewer than 2% of the total pixels. For single-cell resolution platforms, we generated paired high- and low-resolution ST maps for training and validation: 10 μm/pixel (single-cell) and 100 μm/pixel, both covering a 2,560 × 2,560 μm tissue field. For intrinsically low-resolution platforms, only 100 μm/pixel maps over the same field of view were used for model validation. Details for each platform are provided in Supplementary Section 5.

H&E image preprocessing and cell segmentation

Following previous works[12,13], whole-slide H&E images were first converted to RGB and cropped to the tissue-covered area using a simple tissue mask (intensity thresholding and morphological closing). For each whole-slide image, we cropped a field of view of 2,560 × 2,560 μm and tiled it into non-overlapping cellular-scale patches of 160 × 160 μm, consistent with typical local cellular organization in histology. H&E patches with low tissue coverage or strong blur (estimated from gradient magnitude) were discarded. Patches were stored at 0.5 μm/pixel for cell segmentation, and downsampled to 10 μm/pixel (approximately single-cell resolution) for FOCUS training and validation.

Nuclei were segmented from 0.5 μm/pixel patches using a pretrained StarDist2D[70] model, which produces instance-level probability maps and polygonal outlines. Predictions were converted to nuclear masks using default thresholds, small artifacts were removed, and masks were isotropically dilated in a non-overlapping manner to approximate full-cell boundaries. The resulting nuclei and cell masks were stitched back to the tissue field and visually inspected in representative regions.

Pair-wise alignment between H&E images and ST maps

To obtain ground-truth alignment for FOCUS training and validation, we used a two-step landmark-based registration, following previous works[25]. First, H&E images and ST maps were rescaled to a common resolution. Candidate landmark pairs were generated automatically: fiducial beads or printed markers visible in both modalities were detected with a YOLO[71]-based object detector.

Second, these landmarks were manually enhanced in an interactive viewer, removing mismatches and adding points in morphologically complex regions (e.g. large vessels, ducts, region boundaries). The final set of 100-500 landmarks per sample (depending on image size) was used to estimate a global affine transform followed by a thin-plate-spline warp, yielding high-quality registered H&E-ST pairs for FOCUS training and evaluation.

Spatial gene co-expression matrix

We constructed a tissue-type specific spatial gene co-expression matrix as prior knowledge. For each sample of a given tissue context, we flattened the 2D ST map into 1D expression profiles for each gene and computed the PCC between all gene pairs to obtain a sample-level co-expression matrix. We then averaged these matrices across samples to yield the final spatial gene co-expression matrix for that tissue context.

scRNA-seq processing

For each tissue context, we collected scRNA-seq datasets from public repositories (Table S1). Raw count matrices and metadata were converted to AnnData objects and processed with SCANPY[72] package. Following standard quality control (QC), we removed low-quality cells (few detected genes, low total UMI counts, or high mitochondrial fraction) and low-quality genes (expressed in only a small number of cells), with filtering thresholds determined by QC-metric distributions. Counts were then library-size-normalized so that each cell had the same total UMI count. Finally, to enable integration with ST data, we intersected the gene sets of each scRNA-seq dataset with its corresponding ST dataset and retained only the shared genes in the scRNA-seq data.

2. Foundational generative model of FOCUS

2.1 Diffusion framework and multimodal conditioning

FOCUS is a conditional diffusion model that generates high-quality (HQ) ST maps $\mathbf{s_0}$ from multimodal inputs and biological prompts (Extended Fig. 2). HQ ST maps $\mathbf{s_0}$ serve as the generation targets. Raw low-quality (LQ) ST maps $\mathbf{y}$ and paired H&E images $\mathbf{h}$ provide sample-specific conditions. Cell masks $\mathbf{m}$, obtained by segmenting $\mathbf{h}$, impose local structural constraints. Reference scRNA-seq matrices $\mathbf{S}$ of the corresponding tissue context are used to rectify and project LQ ST expression. A pre-computed spatial co-expression matrix (SCM) $\mathbf{M}$ acts as a memory bank encoding gene-gene spatial relationship. Finally, to incorporate biological prior knowledge, we use BioBERT[73] with fully frozen parameters to encode natural language prompts $\mathbf{P}$ describing the platform, species, tissue context, and gene set.

Given a multi-channel HQ ST map $\mathbf{s_0}$ (channels[7] correspond to genes), the forward diffusion process gradually adds Gaussian noise over T diffusion steps following a noise variance schedule $\beta_1, \ldots, \beta_T$. As step increases in the forward process, the input image gets noisier, with the noised image at step t defined as $\mathbf{s}_t = \sqrt{1-\beta_t}\mathbf{s}_{t-1} + \sqrt{\beta_t}\epsilon_t$ where $\epsilon_t \sim \mathcal{N}(\mathbf{0}, \mathbf{I})$ is a standard Gaussian noise vector. A key characteristic of the forward process is its ability to sample $\mathbf{s}_t$ at any arbitrary timestep t in closed form. Using the notation $\alpha_t \coloneqq 1 - \beta_t$ and $\bar{\alpha} := \prod_{j=1}^{t} \alpha_j$, we have

$$\mathrm{q}(\mathbf{s}_t|\mathbf{s}_0) = \mathcal{N}\left(\mathbf{s}_t; \sqrt{\bar{\alpha}_t}\mathbf{s}_0, \right)(1-\bar{\alpha}_t)\mathbf{I}$$

Thus, for sufficiently large T, $\mathbf{s}_T$ approximates an isotropic Gaussian distribution.

The reverse process learns to iteratively remove noise from the noised image $\mathbf{s}_T$. We parameterize the reverse transition

$$p_\theta(\mathbf{s}_{t-1}|\mathbf{s}_t, \mathbf{y}, \mathbf{h}, \mathbf{m}, \mathbf{S}, \mathbf{M}, \mathbf{P}) = \mathcal{N}(\mathbf{s}_{t-1}; \boldsymbol{\mu}_\theta(\mathbf{s}_t, \mathbf{y}, \mathbf{h}, \mathbf{m}, \mathbf{S}, \mathbf{M}, \mathbf{P}), \sigma_t^2\mathbf{I})$$

where θ denotes trainable parameters and σ_t^2 represents the fixed variance. Further, with parameterization, learning μ_θ is replaced by learning the noise $\boldsymbol{\epsilon}_\theta(\mathbf{s}_t, \mathbf{y}, \mathbf{h}, \mathbf{m}, \mathbf{S}, \mathbf{M}, \mathbf{P}, t)$, enabling more stable training. Once trained, we sample HQ ST maps by starting from

[7] Considering the training efficiency, we used the default setting of 5 genes per iteration, consistent with prior works[12].

Gaussian noise $\mathbf{s}_T \sim \mathcal{N}(\mathbf{0}, \mathbf{I})$ and running the learned reverse process conditioned on the multimodal inputs and prompts.

On top of this diffusion backbone and multimodal features from large-scale pretrained encoders, FOCUS introduces three challenge-targeted modules: (**i**) an optimal-transport (OT)-based rectification module that fuses high-sensitivity scRNA-seq with large-scale spatial co-expression knowledge to boost sensitivity; (**ii**) a morphology-expression modulation module that aligns and disentangles ST and H&E features by enforcing local gradient consistency and feature-level correspondence; and (**iii**) a curriculum learning-based constraining module that progressively focuses on complex regions and aligns expression-based and morphology-based cell-cell correlations.

2.2 Multimodal pretraining

FOCUS builds on two large-scale pretrained encoders, including (1) a cross-tissue H&E encoder capturing universal cellular morphology and (2) a cross-platform ST encoder encoding spatial expression patterns, which are used in model training during the reverse diffusion process. Specifically, at a timestep t in the reverse diffusion process, the H&E image $\mathbf{h}$ and reconstructed HQ ST map $\mathbf{s}_t$ are encoded into latent representations $\mathbf{F}_{\mathrm{HE}}$ and $\mathbf{F}_{\mathrm{ST}}$, respectively.

- **Histology encoder.** To obtain universal histological features, we initialize a transformer-based H&E encoder with weights from the pathology foundational model Prov-GigaPath[23]. A lightweight matching layer is appended to map Prov-GigaPath feature dimensions and scales into FOCUS's intermediate latent space.
- **ST encoder.** To capture generic spatial transcriptomic patterns, the ST encoder is initialized from the spatial transcriptomics foundational model scGPT-spatial[24]. As with the histology encoder, a small matching layer performs dimensionality mapping and stabilization, allowing the pre-trained weights to be directly inherited while producing features in the shared latent space.

2.3 OT-based rectification module for sensitivity enhancement

To enhance sensitivity, we design an OT-based rectification module with three coupled components: (1) an OT-based scRNA-ST fusion stage that fuses high-sensitivity scRNA-seq into ST, (2) a spatial gene-correlation strategy that utilizes a gene memory bank incorporating spatial co-expression matrices, and (3) an H&E-guided regional attention mechanism that emphasizes sensitivity in high gradient tissue boundaries of morphologically well-defined regions.

OT-based scRNA-ST fusion

Let $\mathbf{y} \in \mathbb{R}^{\{n_{\{spots\}} \times n_{\{genes\}}\}}$ denote the observed ST expression tensor (reshaped from the spatial map) and $\mathbf{S} \in \mathbb{R}^{\{n_{\{cells\}} \times n_{\{genes\}}\}}$ the matched scRNA-seq matrix. We build a cost matrix $\mathbf{C} \in \mathbb{R}^{\{n_{\{cells\}} \times n_{\{spots\}}\}}$ with entries capturing the squared Euclidean distance between spot and cell expression profiles. Using uniform marginals for spots and cells, we solve an entropically regularized optimal transport problem:

$$\mathbf{\Gamma}^* = argmin_{\mathbf{\Gamma}} < \mathbf{\Gamma}, \mathbf{C} > -\lambda H(\mathbf{\Gamma})$$

where $H(\mathbf{\Gamma})$ is the entropy of the transport plan and λ controls the degree of regularization. We then compute $\mathbf{\Gamma}^*$ with the Sinkhorn algorithm[74] and project the scRNA-seq reference onto the spatial grid:

$$\mathbf{y}' = (\mathbf{\Gamma}^*)^\top \mathbf{S}$$

The rectified expression $\mathbf{y}'$ serves as a globally enhanced ST condition, providing high-sensitivity and denoised gene expression, which is used as input to the following spatial gene-correlation.

The spatial gene-correlation strategy and H&E-guided regional attention mechanism are detailed in Fig. S18 and Supplementary section 6.

2.4 Morphology-expression modulation module for aligning ST with H&E

To align ST with H&E images, we introduce a morphology-expression modulation module (Fig. S19) that **(1)** disentangles shared and unique representations across modalities, and **(2)** enforces local structural consistency across modality-shared representations.

Multimodal disentanglement strategy

Given multimodal feature maps $\mathbf{F}_{\mathrm{OT}}$ and $\mathbf{F}_{\mathrm{CL}}$ encoded from the OT-based rectification module and curriculum learning-based constraining module, we first perform Euclidean normalization,

$$\mathbf{F}_{\mathrm{align}}^{\mathrm{ST}} = \frac{\mathbf{F}_{\mathrm{OT}}}{\| \mathbf{F}_{\mathrm{OT}} \|_2}, \qquad \mathbf{F}_{\mathrm{align}}^{\mathrm{HE}} = \frac{\mathbf{F}_{\mathrm{CL}}}{\| \mathbf{F}_{\mathrm{CL}} \|_2}.$$

Then, we modulate $\mathbf{F}_{\mathrm{align}}^{\mathrm{ST}}$ and $\mathbf{F}_{\mathrm{align}}^{\mathrm{HE}}$ to disentangle shared and unique information between them. For H&E-to-ST modulation, we consider a local $k \times k$ neighborhood around each pixel x in the ST feature map, extracting patches $\mathbf{P}_x^{\mathrm{ST}}$ and $\mathbf{P}_x^{\mathrm{HE}}$ from $\mathbf{F}_{\mathrm{align}}^{\mathrm{ST}}$ and $\mathbf{F}_{\mathrm{align}}^{\mathrm{HE}}$, respectively. A small fully connected filter $\mathbf{f}_\theta$ takes the concatenated patch as input and outputs a local modulation kernel:

$$\mathbf{w}_x = \mathbf{f}_\theta(\mathbf{P}_x^{\mathrm{ST}}, \mathbf{P}_x^{\mathrm{HE}}),$$

which is applied to update the ST feature at x,

$$\tilde{\mathbf{F}}^{\mathrm{ST}}(x) = \mathbf{w}_x * \mathbf{P}_x^{\mathrm{ST}}.$$

A symmetric modulation is applied for ST-to-H&E, yielding $\tilde{\mathbf{F}}^{\mathrm{HE}}$.

We then decompose the modulated features ($\tilde{\mathbf{F}}^{\mathrm{ST}}$ and $\tilde{\mathbf{F}}^{\mathrm{HE}}$) into shared and unique components ($\mathbf{F}_{\mathrm{shared}}^{\mathrm{HE}}$, $\mathbf{F}_{\mathrm{shared}}^{\mathrm{ST}}$, $\mathbf{F}_{\mathrm{unique}}^{\mathrm{HE}}$, $\mathbf{F}_{\mathrm{unique}}^{\mathrm{ST}}$). Based on these features, a disentangling loss

$$\mathcal{L}_{\mathrm{dis}} = -\text{cosine similarity}(\mathbf{F}_{\mathrm{shared}}^{\mathrm{HE}}, \mathbf{F}_{\mathrm{shared}}^{\mathrm{ST}}) + \gamma \text{cosine similarity}(\mathbf{F}_{\mathrm{unique}}^{\mathrm{HE}}, \mathbf{F}_{\mathrm{unique}}^{\mathrm{ST}})$$

maximizes cosine similarity between shared features while encouraging uniqueness of modality-specific components ($\gamma > 0$). The final multimodal fused representation

$$\mathbf{F}_{\mathrm{CM}} = [\, \mathbf{F}_{\mathrm{shared}}^{\mathrm{HE}}, \mathbf{F}_{\mathrm{shared}}^{\mathrm{ST}}, \mathbf{F}_{\mathrm{unique}}^{\mathrm{HE}}, \mathbf{F}_{\mathrm{unique}}^{\mathrm{ST}} \,]$$

serves as a rich conditioning input to the diffusion reverse process, providing structurally aligned and biologically disentangled guidance for generating HQ ST maps.

Local gradient constraining

Then, we conduct local gradient constraining on the modality-shared features $\mathbf{F}_{\text{shared}}^{\text{HE}}$ and $\mathbf{F}_{\text{shared}}^{\text{ST}}$ for alignment between H&E and ST maps. Specifically, gaussian noise is first added to $\mathbf{F}_{\text{shared}}^{\text{ST}}$ and the result is re-normalized to form a local ring distribution on the hypersphere, improving robustness to perturbations.

We then map the features to modality-independent structural maps $\mathbf{S}^{\text{ST}}$ and $\mathbf{S}^{\text{HE}}$ via shared convolutional layers. Non-cellular regions in the H&E map are masked out with the cellular mask to yield a boundary-emphasized map $\mathbf{S}_{\text{cell}}^{\text{HE}}$. Horizontal and vertical Sobel operators are applied to compute gradient fields $\nabla\mathbf{S}^{\text{ST}}$ and $\nabla\mathbf{S}_{\text{cell}}^{\text{HE}}$.

A spatial transformer network predicts a deformation field $\boldsymbol{\phi}$ that warps ST space to H&E space,

$$\mathbf{S}^{\text{ST}\to\text{HE}} = \mathbf{S}^{\text{ST}} \circ \boldsymbol{\phi}.$$

Based on $\nabla\mathbf{S}^{\text{ST}\to\text{HE}}$ and $\nabla\mathbf{S}_{\text{cell}}^{\text{HE}}$, we optimize three gradient-based consistency terms. First, the normalized gradient field (NGF) loss constrains edge orientations:

$$\mathcal{L}_{\text{NGF}} = \int_{\Omega} 1 - \frac{\langle \nabla\mathbf{S}^{\text{ST}\to\text{HE}}, \nabla\mathbf{S}_{\text{cell}}^{\text{HE}} \rangle + \delta}{\parallel \nabla\mathbf{S}^{\text{ST}\to\text{HE}} \parallel \ \parallel \nabla\mathbf{S}_{\text{cell}}^{\text{HE}} \parallel + \delta} \, dx,$$

where δ is a stability constant.

Second, the gradient magnitude consistency (GMC) loss aligns edge strengths:

$$\mathcal{L}_{\text{GMC}} = \int_{\Omega} \left\| \parallel \nabla\mathbf{S}^{\text{ST}\to\text{HE}} \parallel - \parallel \nabla\mathbf{S}_{\text{cell}}^{\text{HE}} \parallel \right\|^2 dx.$$

Third, we define gradient magnitude similarity

$$GMS(x) = \frac{2a(x)b(x) + c}{a(x)^2 + b(x)^2 + c},$$

where $a(x) = \parallel \nabla\mathbf{S}^{\text{ST}\to\text{HE}}(x) \parallel$, $b(x) = \parallel \nabla\mathbf{S}_{\text{cell}}^{\text{HE}}(x) \parallel$ and c prevents division by zero. The gradient magnitude stability constraint (GMSC) is the standard deviation of GMS over Ω,

$$\mathcal{L}_{\text{GMSC}} = \text{Std}_{x\in\Omega}[GMS(x)],$$

penalizing abrupt local variations in gradient magnitude.

A boundary weighting map $\mathbf{W_{bnd}}$ is derived from the normalized gradient of the distance transform of the cellular mask, emphasizing structure around cell contours. The final structural loss is

$$\mathcal{L}_{\text{struct}} = \sum_{x} \mathbf{W_{bnd}}(x)(\mathcal{L}_{\text{NGF}}(x) + \mathcal{L}_{\text{GMC}}(x) + \mathcal{L}_{\text{GMSC}}(x)).$$

2.5 Curriculum learning-based constraining module for profiling imputation in complex regions

We balance profiling performance across tissues with varying complexity by **(1)** a cellular patch selection and multi-scale fusion scheme, and **(2)** an ST-H&E constraining strategy on cell-cell correlations.

Cellular patch selection and multi-scale fusion scheme

The H&E image $\mathbf{h}$ [2,560 × 2,560 μm] is cropped into non-overlapping cellular-level patches $\{\mathbf{p}_i\}$ [160×160 μm], which are separately encoded by the histology encoder into feature maps $\mathbf{F}_{\text{HE}}$ and $\{\mathbf{F}_i^{\text{cell}}\}$. For each patch, we compute the complexity score

$$\mathrm{c}_i = \mathrm{Comp}(\mathbf{p}_i),$$

As defined in Section 6 in Methods. Curriculum learning is implemented by increasing a complexity threshold over training so that early iterations focus on simple patches and later iterations progressively incorporate more complex regions. At each stage, only patches with c_i above the current threshold are retained, yielding selected cellular-scale features $\mathbf{F}_{\text{cell}}$.

To obtain overall H&E features $\mathbf{F}_{\text{CL}}$, we fuse $\mathbf{F}_{\text{cell}}$ with tissue-scale features $\mathbf{F}_{\text{HE}}$ via cross-attention. After pixel flattening, queries $\mathbf{Q}$ is derived from tissue-scale features and keys/values $\mathbf{K}, \mathbf{V}$ from cellular-scale features, with learnable projections W_Q, W_K, W_V , producing

$$\mathbf{F}_{\text{CL}} = \mathrm{Attention}(\mathbf{Q}W_Q, \mathbf{K}W_K, \mathbf{V}W_V).$$

ST and H&E constraining

To mitigate signal mixing in highly complex regions, we identify the cellular-level patch with the highest complexity score

$$\mathbf{p}^* = arg\ \max_{\mathbf{p}_i}\ \mathrm{c}_i,$$

and treat it as the patch most prone to expression mixing.

For each cell j identified within the cell segmentation mask of patch $\mathbf{p}^*$, we compute its spatially averaged embeddings using the modality-specific encoders, i.e., $\mathbf{e}_j^{\mathrm{HE}}$ from the H&E patch and $\mathbf{e}_j^{\mathrm{ST}}$ from the corresponding ST.

We then compute cell-cell correlation matrices for each modality ($\mathbf{C}^{\mathrm{HE}}$ for H&E image and $\mathbf{C}^{\mathrm{ST}}$ for ST) for cells in patch $\mathbf{p}^*$. The (j,k) entry is the Pearson correlation coefficient between the embeddings of cells j and k, i.e., $\mathbf{C}_{jk}^{\mathrm{HE}} = \mathrm{PCC}\left(\mathbf{e}_j^{\mathrm{HE}}, \mathbf{e}_k^{\mathrm{HE}}\right)$ for H&E and $\mathbf{C}_{jk}^{\mathrm{ST}} = \mathrm{PCC}(\mathbf{e}_j^{\mathrm{ST}}, \mathbf{e}_k^{\mathrm{ST}})$ for ST.

Finally, we encourage the cell-cell correlation matrices across modalities to be similar, allowing histology-derived context to correct transcriptomic miss-profiling in complex regions. We impose a cosine-similarity-based consistency loss

$$\mathcal{L}_{\mathrm{consis}} = 1 - \frac{cosine\ similarity(\mathbf{C}^{\mathrm{HE}}, \mathbf{C}^{\mathrm{ST}}) + 1}{2},$$

where the cosine similarity is computed after vectorizing the correlation matrices.

2.6 Cross-challenge coordination

To explicitly model cross-challenge coupling, we place a lightweight cross-challenge coordinator within the diffusion U-Net to mediate interactions among the expert modules targeted to individual challenges.

For each module m, we first compress its spatial feature map $\mathbf{F}_m \in \mathbb{R}^{C_m \times H \times W}$ into a fixed-dimensional expert token $\mathbf{z}^{(m)} \in \mathbb{R}^d$ using global pooling followed by a linear projection. The set of tokens $\{\mathbf{z}^{(m)}\}$ is then processed by a multi-head attention block, allowing each module to query the others and aggregate complementary information. This produces

updated tokens $\hat{\mathbf{z}}^{(m)}$ that encode cross-challenge context, such as how misalignment interacts with local resolution or tissue heterogeneity.

Each updated token is mapped, via a multilayer perceptron, to channel-wise scaling and offset parameters $(\boldsymbol{\alpha}_m, \boldsymbol{\beta}_m)$ with the same dimensionality as $\mathbf{F}_m$. The original feature map is recalibrated in a feature-wise linear modulation (FiLM)-like manner,

$$\mathbf{F}'_m = \boldsymbol{\alpha}_m \odot \mathbf{F}_m + \boldsymbol{\beta}_m,$$

and a learnable residual gate mixes $\mathbf{F}'_m$ with $\mathbf{F}^{(m)}$ to preserve module specialization and maintain training stability. The coordinated features $\mathbf{F}'_m$ are finally injected back into the U-Net as residuals to guide subsequent diffusion steps.

3. Challenge coordination score

To indicate the detection and activation status of each challenge in FOCUS, we define a challenge coordination score. Specifically, for module m (sensitivity, alignment, or complexity), the score γ_m is computed from the channel-wise scaling parameters $\boldsymbol{\alpha}_m$ associated with the module output features $\mathbf{F}_m$. For a module m with C_m channels, we define

$$\gamma_m = sigmoid\left(\frac{1}{C_m}\sum_{c=1}^{C_m} \alpha_{m,c}\right).$$

A challenge is considered activated when $\gamma_m > 0.5$, indicating that the corresponding module is actively detecting and jointly mitigating that challenge.

For the spatial resolution challenge, the score is derived directly from the spatial resolution of the input ST. We mark the resolution challenge as activated when the map resolution is finer than the single-cell resolution threshold of $10\ \mu$m/pixel.

4. Dataset splitting

Training and *internal validation*: All platforms with high-resolution[8] (HR) ST-H&E pairs were used for model training, with over 0.53 million (80% of total HR ST-H&E pairs)

[8] Due to the resolution requirement of the generation target in training diffusion models, we only included platforms providing single-cell resolution (i.e., ≤ 10 μm/pixel[75]) ST maps.

patches, including VisiumHD (144,384 patches), Stereo-seq (8,396 patches), BMK S1000 (24,576 patches), CosMx (18,227 patches), and Xenium (339,148 patches). For internal validation of ST challenges, we included around 1.09 million ST-H&E patches across nine platforms, except Open-ST as external validation.

External validation: we fine-tuned and tested FOCUS on the previously unseen Open-ST platform and an unseen clinical dataset of PCP (Xenium), consisting of 101,120 and 6,144 ST-H&E patches, respectively.

5. Foundational training and fine-tuning

Overall, the learning process of FOCUS comprises two stages: (1) cross-platform training with paired H&E-ST data to jointly address diverse challenges across ST platforms, and (2) lightweight fine-tuning on previously unseen platforms or tissue context to enhance real-world generalization.

5.1 Cross-platform training

FOCUS follows a conditional diffusion training paradigm, using HQ ST as the generation target and LQ ST, H&E, cell masks, scRNA-seq, and spatial co-expression priors as the primary conditions. During training, Gaussian noise is added to the HQ ST map $\mathbf{s}_0$ according to the diffusion schedule to obtain a noisy sample $\mathbf{s}_t$. The model then predicts the injected noise $\boldsymbol{\epsilon}_t$ and progressively denoises $\mathbf{s}_t$ under multimodal constraints and biological prompts.

The overall training objective for the conditional diffusion model is a weighted multi-term loss. The primary term is the standard diffusion-based noise-prediction loss on HQ ST. Additional terms encourage (i) alignment with tissue structures, and (ii) consistency between morphology-based and expression-based cell-cell relationships (see Sections 2.4-2.5 in Methods). The overall loss for training the conditional diffusion model ST super-quality is formulated as

$$\mathcal{L}_{\text{all}} = \lambda_1 \mathcal{L}_{\text{charb}} + \lambda_2 \mathcal{L}_{\text{struct}} + \lambda_3 \mathcal{L}_{\text{dis}} + \lambda_4 \mathcal{L}_{\text{consis}},$$

$$\text{where } \mathcal{L}_{\text{charb}} = \sqrt{(\boldsymbol{\epsilon}_\theta(\mathbf{s}_t, \mathbf{y}, \mathbf{h}, \mathbf{m}, \mathbf{S}, \mathbf{M}, \mathbf{P}, t) - \epsilon_t)^2 + \gamma^2}$$

In the above equation, Charbonnier loss $\mathcal{L}_{\text{charb}}$ is a smoother transition between $\mathcal{L}_1$ and $\mathcal{L}_2$ loss, facilitating more steady and accurate convergence during training. γ is a known constant and λ_1 , λ_2 , λ_3 , and λ_4 represent weights for four losses.

Implementation details. We trained FOCUS for 2000 epochs on seven NVIDIA RTX V100 32 GB GPUs, with a batch size of 4 and a learning rate 0.0001 with the AdamW optimizer[76] with the weight decay. Following the sampling strategy in previous works[77], our method used a sample step of 1,000 in both forward and reverse processes. Key hyper-parameters are in Table S8, which were tuned to achieve the best performance in all challenges.

5.2 Fine-tuning for unseen platforms and tissue context

To adapt FOCUS to previously unseen ST platforms or tissue contexts, we employ a freeze-update fine-tuning strategy that preserves foundational cross-platform representations while enabling flexible, data-efficient specialization in new domains.

Specifically, to maintain the generic histological and ST representations acquired during large-scale cross-platform training, we keep the U-Net encoder frozen. Only higher-level components are updated, including the decoder, the four expert modules, and the conditional fusion/match layers.

In addition, to achieve stable fine-tuning that preserves pre-trained features during transfer to unseen platforms or tissues, we apply Low-Rank Adaptation (LoRA) inside the expert modules. For each weight matrix $\boldsymbol{W} \in \mathbb{R}^{d\times h}$ in a module, we freeze $\boldsymbol{W}$ and learn a low-rank update

$$\widehat{\boldsymbol{W}} = \boldsymbol{W} + \mathbf{AB},$$

where $\mathbf{A} \in \mathbb{R}^{d\times r}$ and $\mathbf{B} \in \mathbb{R}^{r\times h}$ with $r \ll \min(d, h)$. Only $\mathbf{A}$ and $\mathbf{B}$ are trainable, providing lightweight adaptation while preserving the geometry of the pre-trained features.

Finally, to flexibly control modules and achieve fine-tuning tailored to specific tasks, we employ a routing mechanism based on expert tokens to combine modules on demand. In detail, we weigh up the residual updates of each module based on the expert tokens generated by the adapter, and allow the corresponding expert modules to be blocked

when there is no corresponding demand. Each expert module $\mathbf{M}_i$ produces a residual update $R_i(\mathbf{F})$ to the shared latent features $\mathbf{F}$. A routing network reads the prompt and outputs coefficients α_i for all modules. The combined residual is

$$\mathbf{F}' = \mathbf{F} + \sum_i \alpha_i R_i(\mathbf{F})$$

Modules corresponding to challenges absent in each platform are effectively disabled by setting $\alpha_i = 0$.

6. Tissue complexity definition

To evaluate how well FOCUS corrects miss-profiling in regions of high complexity, we define complexity as a composite index summarizing two H&E-derived properties: (1) cell abundance (how crowded the patch is) and (2) morphological diversity (how heterogeneous the cells are). Formally, the overall complexity $C \in [0,1]$ is a convex combination of a normalized density score $D_{\text{norm}} \in [0,1]$ and a normalized heterogeneity score $H_{\text{norm}} \in [0,1]$:

$$C = \alpha\, D_{\text{norm}} + (1 - \alpha)\, H_{\text{norm}},$$

where α (=0.5) is a balancing weight between cell density and heterogeneity score. High C values, therefore, indicate patches that are both cell-dense and morphologically diverse, commonly associated with biologically active or pathologic regions (e.g., highly cellular, pleomorphic tumor areas).

Definitions of the cell density and heterogeneity score are as follows.

6.1 Cell density score

Cell density is quantified by normalizing the number of segmented cells N in a patch to an upper bound $N_{\max}$ on expected cell counts, yielding a score that increases with cellular crowding:

$$D_{\text{norm}} = \min\left(\frac{N}{N_{\max}}, 1\right).$$

Note that the cell number upper bound $N_{\max}$ is defined as:

$$N_{\max} = \frac{A_{\mu m^2}}{\pi r_{\min}^2},$$

where $A_{\mu m^2}$ is the patch area in μm^2, and $r_{\min}$ is a lower-bound on cell radius (set to 3 μm as a small lymphocyte-size cell).

6.2 Cell heterogeneity score

Cell heterogeneity is jointly determined by cell shape, size and texture variety, defined as follows.

Shape variety score: Shape heterogeneity captures variability in cellular morphology by summarizing the dispersion of three descriptors: eccentricity z_e, solidity z_s and circularity z_c , into a single score. The combined dispersion is:

$$\Delta_{\text{shape}} = \frac{|\, z_e \,| + |\, z_s \,| + |\, z_c \,|}{3}$$

and the corresponding heterogeneity score is:

$$S_{\text{shape}} = \frac{\Delta_{\text{shape}}}{1 + \Delta_{\text{shape}}},$$

where larger S_{shape} reflects more irregular and diverse nuclear shapes.

Size variety score: Size heterogeneity measures variation in nuclear size using the variability of log-transformed nuclear area $z_{\log A}$ and equivalent diameter z_d . The variability is given by:

$$\Delta_{\text{size}} = \frac{|\, z_{\log A} \,| + |\, z_d \,|}{2}$$

and the normalized score is:

$$S_{\text{size}} = \frac{\Delta_{\text{size}}}{1+\Delta_{\text{size}}},$$

Where patches with a wide range of nuclear sizes attain higher scores.

Texture variety score: The texture heterogeneity score evaluates diversity in chromatin staining patterns. It uses the deviations in hematoxylin entropy z_h and staining intensity variance z_v:

$$\Delta_{\text{texture}} = \frac{|\ z_h\ | + |\ z_v\ |}{2}$$

with the corresponding score:

$$S_{\text{texture}} = \frac{\Delta_{\text{texture}}}{1 + \Delta_{\text{texture}}},$$

where a higher S_{texture} indicates heterogeneous chromatin organization.

Combined heterogeneity: The overall heterogeneity score is obtained as a weighted combination of the shape, size and texture heterogeneity components and is constrained to lie in $[0, 1]$:

$$H_{\text{norm}} = \frac{w_{\text{shape}} S_{\text{shape}} + w_{\text{size}} S_{\text{size}} + w_{\text{texture}} S_{\text{texture}}}{w_{\text{shape}} + w_{\text{size}} + w_{\text{texture}}},$$

where w_{shape}, w_{size}, and w_{texture} are all set to 1.

7. PCP data collection

Patients recruiting

Three PCP patients providing specimens for Xenium analysis were recruited from the Department of Neurosurgery, West China Hospital, Sichuan University (ethics approval no. 20211047A). All patients were diagnosed with intracranial tumors according to the WHO 2021 diagnostic criteria. Tumor tissues were obtained by surgical resection, and none of the patients received any treatment before surgery.

PCP tissue sequencing on Xenium

We then prepared Formalin-Fixed, Paraffin-Embedded (FFPE) samples of patients with PCP, estimated RNA integrity using the percentage of DV200, and evaluated tissue morphology using H&E and DAPI staining before chip testing. The chip manufacturing method is based on the Xenium user guides CG000578 and CG000580 from 10X Genomics. In short, the sample was cut into 5 μm paraffin sections and attached to a Xenium chip. After deparaffinization and decrosslinking the sections, a human 5K panel was used. The probe and sample were hybridized overnight at 50 °C for 20 hours using CG000582 method, and the probe end was connected to the target gene and washed

with PBS-T. Then they were extended at 37 °C for 2 hours and obtain highly specific DNA probes through rolling ring replication. Similarly, amplify at 37 °C for 2 hours to obtain more DNA amplification products. Then, the background fluorescence was chemically quenched to reduce the tissue's own fluorescence. The tissue slices were stained with DAPI nuclear staining, and the chip was placed in an imaging box according to the steps of CG000584. Finally, it was run on a Xenium detection instrument (PN-1000529).

CODEX preparation and imaging

We used tissue sections adjacent to those used for Xenium sequencing for CODEX. Carrier-free monoclonal or polyclonal anti-human antibodies were purchased (Table S9) and verified using immunofluorescence (IF) staining in multiple channels. After screening, antibodies were conjugated using an Akoya Antibody Conjugation Kit (Akoya Biosciences) with a barcode (Akoya Biosciences) assigned according to the IF staining results. Several common markers were directly purchased through Akoya Biosciences. CODEX staining and imaging were performed according to the manufacturer's instructions (CODEX user manual, Rev C). In brief, 5-μm FFPE sections were placed on coverslips coated with APTES (Sigma, 440140) and baked at 60 °C overnight before deparaffinization. The next day, tissues were incubated in xylene, rehydrated in ethanol, and washed in ddH_2O before antigen retrieval with TE buffer, pH 9 in boiling water for 10 min in a rice cooker. The tissue samples were then blocked using blocking buffer (CODEX staining kit) and stained with the marker antibody panel to a volume of 200 μl for 3 hours at room temperature in a humidified chamber. Imaging of the CODEX multicycle experiment was performed using a Keyence fluorescence microscope (model BZ-X810) equipped with a Nikon CFI Plan Apo λ ×20/0.75 objective, a CODEX instrument (Akoya Biosciences), and a CODEX instrument manager (Akoya Biosciences). The raw images were then stitched and processed using the CODEX processor (Akoya Biosciences).

8. Cell type annotation based on ST

For PCP (Xenium) and HNSCC (Open-ST) data, we conducted cell type annotation using ST data. Based on pre-processed ST data, highly variable genes were selected using SCANPY pp.highly_variable_genes, PCA was computed using SCANPY tl.pca, and a

KNN graph was built in PCA space using SCANPY pp.neighbors. Cells were embedded with SCANPY tl.umap and clustered on the kNN graph with SCANPY tl.leiden. Markers were identified using SCANPY tl.rank_genes_groups with method set to wilcoxon, and cell clusters were manually annotated by matching the top-ranked markers to canonical lineage and state markers curated from the literature.

9. Neighborhood enrichment analysis with ST

We used Squidpy package[78] to quantify spatial neighborhood enrichment between enhanced cell populations in primary HNSCC tumors and matched metastatic lymph nodes. For each sample, a spatial connectivity graph was built from spot coordinates. Neighborhood enrichment scores were computed by comparing the observed number of neighboring spot pairs for each cell-type pair with a null distribution generated by random permutation of cell labels. The resulting enrichment matrices were visualized as heatmaps, with the significant number denoting the number of cell-type pairs with statistically significant enrichment.

10. Cell co-occurrence analysis with ST

In PCP enhanced ST maps, we assessed distance-dependent spatial relationships between neutrophils and other cell populations using Squidpy package[78]. For increasing distance around each neutrophil, we calculated the ratio of the conditional probability of observing a given cell type near neutrophils to its marginal probability in the tissue. Co-occurrence curves thus report enrichment (score > 1) or depletion (score < 1) of each cell population around neutrophils across spatial scales.

11. Spatial niches identification with ST

Spatial niches were defined using the radius-based neighborhood workflow implemented in the SCIMAP package[79]. For each cell, we computed the normalized composition of neighboring cell types within a fixed radius to generate a neighborhood-by–cell-type matrix, which was subsequently subjected to unsupervised clustering (k = 6) to identify recurrent spatial niches in the PCP microenvironment. The relative abundance of

annotated cell populations within each niche was summarized and visualized using stacked barplots.

Data availability:

The collected cross-platform multimodal data (including paired ST and H&E images with scRNA-seq references, as well as the segmented cell masks and pre-computed spatial gene co-expression matrix) from public sources are summarized in Tables S1-3. These curated cross-platform multimodal datasets will be made publicly available upon acceptance.

Restrictions apply to the availability of the raw in-house data of PCP (Xenium), which was used with institutional permission through ethics approval for the current study, and are thus not publicly available. Please email all requests for academic use of raw and processed data to the corresponding author. All requests will be evaluated based on institutional and departmental policies to determine whether the data requested is subject to intellectual property or patient privacy obligations. Data can only be shared for non-commercial academic purposes and will require a formal material transfer agreement.

Code availability:

Codes are available at https://github.com/LHY1007/FOCUS/.

Acknowledgements:

This work was supported by the NIHR Brain Injury MedTech Co-operative, the NIHR Cambridge Biomedical Research Centre (NIHR203312), Addenbrooke's Charitable Trust. This work presents independent research funded by the National Institute for Health and Care Research (NIHR). The views expressed are those of the author(s) and not necessarily those of the NHS, the NIHR or the Department of Health and Social Care. This work was supported by the National Natural Science Foundation of China (32571681). Xiaofei Wang reports financial support by China Scholarship Council. Chao Li reports financial support by the Guarantors of Brain.

Competing interests:

None.